Creep and Microstructural Characterization of Advanced Austenitic Stainless Steel Alloy 709

A Thesis
Presented in Partial Fulfillment of the Requirement for the
Degree of Master of Science
with a
Major in Material Science and Engineering
in the
College of Graduate Studies
University of Idaho
by
Martin Taylor

Major Professor: Indrajit Charit, Ph.D.

Committee Members: Krishnan Raja, Ph.D.; Robert Stephens, Ph.D.;
Gabriel Potirniche, Ph.D.

Department Administrator: D. Eric Aston, Ph.D

August 2018

Authorization to Submit Thesis

This thesis of Martin Taylor, submitted for the degree of Master of Science with a major in Material Science and Engineering and titled "Creep and Microstructural Characterization of Advanced Austenitic Stainless Steel Alloy 709," has been reviewed in final form. Permission, as indicated by the signatures and dates given below, is now granted to submit final copies to the College of Graduate Studies for approval.

Major Professor _____ Date _____
Indrajit Charit, Ph.D

Committee Members _____ Date _____
Krishnan Raja, Ph.D

_____ Date _____
Robert Stephens, Ph.D

_____ Date _____
Gabriel Potirniche, Ph.D

Department Administrator _____ Date _____
D. Eric Aston, Ph.D

Abstract

Alloy 709 is a potential material for structural applications in advanced nuclear reactors such as sodium cooled fast reactors. It is a promising austenitic stainless steel that exhibits excellent high temperature creep strength, fatigue crack growth resistance, and corrosion resistance. However, fundamental information on the creep and fatigue behavior of the alloy is sparse. In this study, creep tests on Alloy 709 were performed at 600°C and 700°C under applied stresses of 125 to 250 MPa. The alloy exhibited a brief primary, insignificant secondary and prolonged tertiary creep stages. The stress exponent (n) of 6.7 and 5.9 was obtained from the Norton plots at 600°C and 700°C, respectively. Transgranular fracture was observed in creep-ruptured specimens. The Norton constants calculated in this study were utilized in a parallel collaborative effort involving finite element analysis models to predict creep-fatigue crack growth behavior of Alloy 709.

Thermal aging of Alloy 709 was carried out at 650°C for 3 and 6 months to study the effects of the detrimental σ phase and $M_{23}C_6$ precipitates on the creep and tensile strength of the alloy. The overall creep behavior was described by the Bird-Mukherjee-Dorn relation. Dislocation climb was found to be the primary mechanism of creep deformation in Alloy 709. Microstructural analyses were carried out for the as-received and crept specimens using optical microscopy, scanning electron microscopy (SEM), electron backscattered diffraction (EBSD), and transmission electron microscopy (TEM). Some microstructural results (optical and EBSD) of the creep-fatigue crack growth and fatigue crack growth are also discussed.

Acknowledgments

The guidance and support of Dr. Indrajit Charit was pivotal for me through the years here and I am extremely thankful for it. His encouragement gave me the drive to further my education and push my knowledge in the materials field. I would like to thank my committee members, Dr. Krishnan Raja, Dr. Robert Stephens, and Dr. Gabriel Potirniche for their assistance and insight through my time here.

I would like to acknowledge Dr. Michael Glazzoff (Idaho National Lab) for his computational insights. His computational expertise and access to PRISMA and ThermoCalc were very helpful in understanding the alloy.

I would like to thank the U.S Department of Energy, DOE-NEUP grant (#DE-NE0008443) entitled “Characterization of Creep-Fatigue Crack Growth in Alloy 709 and Prediction of Service Lives in Nuclear Reactor Components” for funding this project.

I would like to acknowledge Tom Williams and Anumat Sittiho for their assistance in learning to use the scanning electron microscope (SEM), transmission electron microscope (TEM), X-ray diffraction (XRD), energy dispersive spectroscopy (EDS) and electron backscatter diffraction (EBSD). I would also like to thank Nick Shaber, Jose Ramirez, and Harrison Pugesek for their insights and studies on Alloy 709.

I would like to acknowledge Arnab Kundu and Sean Instasi for their assistance in proper lab techniques and support. I would like to thank Alan Carter (Colorado School of Mines) for the advice for an aging schedule.

I would like to thank Charles Cornwall for his hard work and expertise in machining the creep and tensile specimens in a timely manner.

Dedication

I want to dedicate this thesis to my family and my friends for their support and encouragement throughout my education. I know that without their support, I would not be here today. Thank you!

Table of Contents

List of Figures

List of Tables

Chapter 1. Background and Literature Review

1.1 Introduction

As the world's energy consumption continues to rise, the need for more efficient nuclear and coal power plants has been an area of great importance. Generation IV reactors including Sodium-cooled Fast Reactors (SFR), Gas-cooled Fast Reactors (GFR), Lead-cooled Fast Reactors (LFR), Molten Salt Reactors (MSR), and Very High Temperature Reactors (VHTR), all require materials that can serve under high temperature, greater radiation doses and extremely corrosive environment. One of the important requirements for the structural materials used under such high temperature conditions for prolonger duration of time is superior high temperature mechanical properties. The SFR has a maximum operating temperature of 500 – 550^{o}C [1]. The life of these reactors are expected to last over 60 years.

The increase in operating temperatures of nuclear plants has led to efforts in improving the creep resistance of austenitic stainless steels. Alloy 709, originally developed by Nippon Steel (Tokyo, Japan) and marketed as NF709, is a novel austenitic stainless steel based on a Fe-20Cr-25Ni base composition. It exhibits excellent high temperature creep, yield, and fatigue strength, with excellent corrosion resistance [2, 3]. However, fundamental information on the creep behavior of the alloy is still sparse.

1.1.2 Objective

The objectives of this thesis research are as summarized below.

- Understand the microstructural characteristics of Alloy 709.
- Determine how the evolution of the materials microstructure at high temperatures can have a significant effect on the mechanical properties, such as creep, fatigue, and creep-fatigue behavior.
- Use Norton's law and Bird-Mukherjee-Dorn equations to evaluate the parametric dependencies such as stress exponent to help determine the creep mechanisms of creep under these conditions.
- Determine the mechanism of the crack growth for fatigue and creep-fatigue by studying microstructure of such samples.

1.2 Sodium-cooled Fast Reactors

The SFR is at the forefront of the Generation IV reactors considered in the US due to its reasonable coolant temperature and low pressure. A schematic SFR design is shown in Figure 1.1. The liquid sodium coolant allows a high power density with a low coolant volume, all at near atmospheric pressures [4]. The boiling point of liquid sodium is over 850^{o}C so the operating temperature of 550 ^{o}C allows a grace period of several hours in loss of coolant accidents (LOCA) [5]. Additionally, there is no hydrogen generation from the sodium coolant which further increases the safety features of this design.

Sodium, however, chemically reacts with air and water which requires the coolant to be in a closed system. Keeping the coolant contained requires materials that can maintain excellent mechanical properties at high temperatures, such as sodium compatibility, weldability, easily machinable, and can handle irradiation doses of 10 – 200 displacements per atom (dpa) [6].

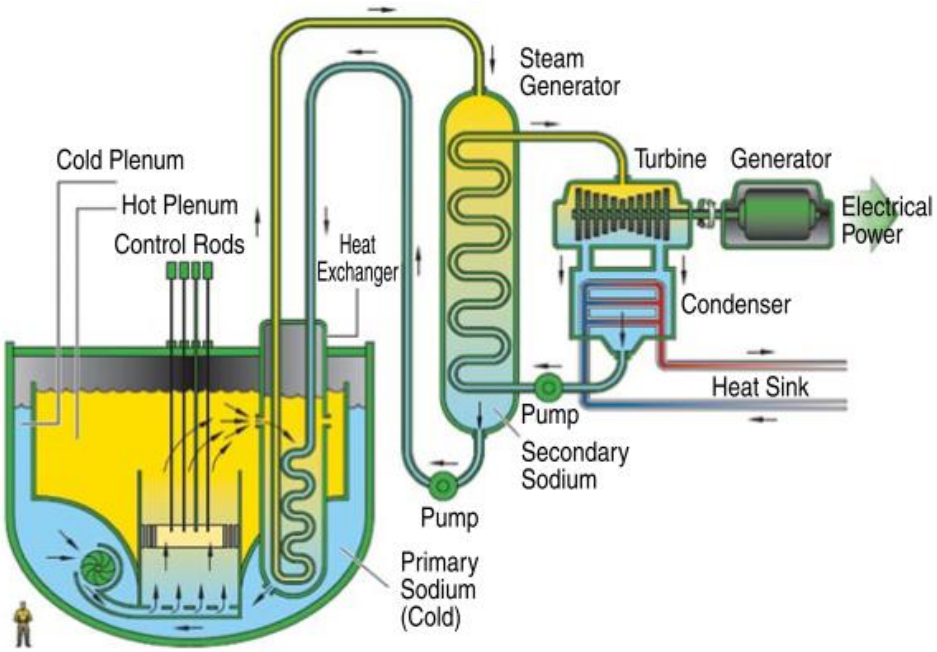

Figure 1.1. Power generation section of a Sodium-cooled Fast Reactor [1]

1.3 Austenitic Stainless Steel

Austenitic stainless steels are used widely because of their corrosion resistance, high temperature strength, and economic feasibility of the alloys. Austenitic stainless steels are known for a wide variety of compositions but is primarily a Fe-Cr-Ni alloy. The chromium content is generally over 12 wt% for the alloy to form a passive chromium oxide film. Nickel also improves the corrosion resistance but primarily is used to increase the high temperature

strength of the material and to stabilize austenite. The FCC lattice provides for a reduced diffusivity because of the close packed structure compared to ferritic steels with more open BCC lattice structure. A significant amount of research on optimizing the composition of austenitic stainless steels for high temperature applications have been carried out and there are a number of different grades of austenitic stainless steels available in the market [7].

Austenite, ferrite and martensite are the primary phases found in stainless steels. The phase of a stainless steel depends on the composition and the thermal process in preparing the material. Martensite forms when austenite is quenched rapidly leaving the material in a metastable phase that significantly increases the hardness of the material. The alloying elements generally fall under two categories, austenite stabilizers and ferrite stabilizers [8]. Austenite has a FCC crystal structure and is stabilized by N, C, Ni, Mn, and Cu. Ferrite has a BCC crystal structure and is stabilized with addition of Cr, Si, Mo, and Nb. The Fe-Cr-Ni ternary diagram is an empirical guide to determine what phase(s) to expect at a certain composition in stainless steels. Note a 20/25 is within the austenite region of the ternary diagram.

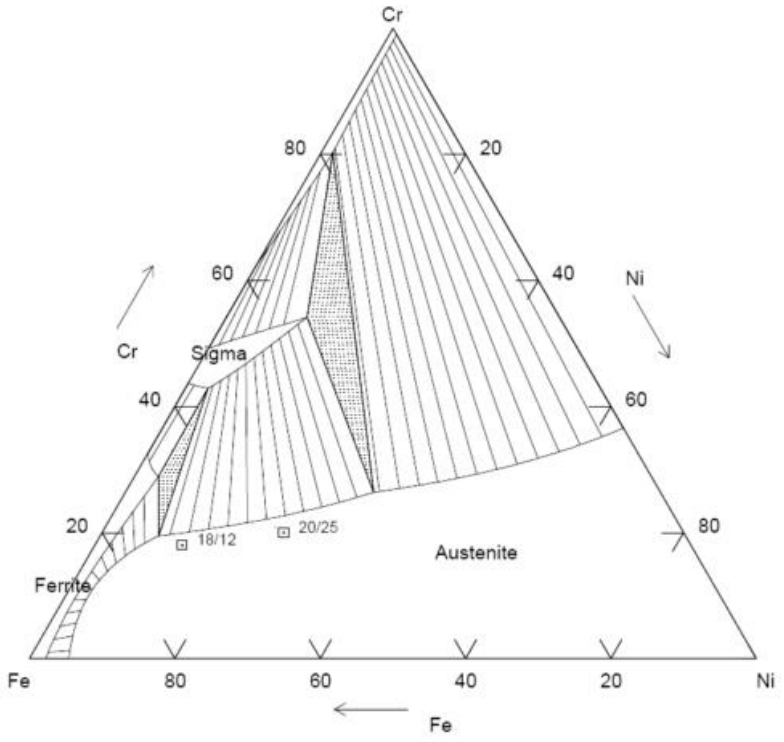

Figure 1.2. Fe-Cr-Ni ternary diagram showing the effect of the nickel and chromium content on the stability of austenite [9]

The more densely packed FCC structure of austenite increases the creep properties of the material making it the ideal phase for high temperature applications. The other alloying elements in common austenitic stainless steels have their advantages and disadvantages.

Chromium – a crucial alloying element in stainless steels that improves hardenability, strength, wear resistance, and increase the corrosion resistance. It can be found forming precipitates like $M_{23}C_6$, Cr_2N, M_6C, Z-phase, σ phase, etc. [10, 11].

Nickel – is crucial for stabilizing austenite. It also aids in solid solution strengthening which increases the impact strength and toughness. Nickel also contributes to the corrosion resistance of the alloy. However, hydrogen pick up can become an issue in the presence of nickel.

Manganese – is added to increase the hardenability, ductility, and wear resistance of the stainless steel. It helps to prevent detrimental iron sulfides increasing the high temperature strength. Mn is a cheaper austenite stabilizer than Ni; so it can reduce the cost of the stainless steel [12]. The composition of Mn in high temperature stainless steels is kept low because it can decrease the creep rupture life.

Molybdenum – is often added to stainless steels because it increases the high temperature strength, improves creep resistance due to solid solution hardening, and can help in corrosion resistance particularly improving pitting resistance [13]. In some stainless steels tungsten is added over molybdenum because tungsten forms precipitates that have a slower response to creep along with imparting solid solution strengthening [10]. Also, tungsten in steel composition is known to create reduced activation steels.

Niobium – forms a very stable Nb(CN) precipitate that is beneficial for pinning mobile dislocations, and removing carbon from the matrix helping the corrosion resistance. Nb also has low neutron absorption cross-section (low activation) [10]. The Nb(CN) precipitates are very stable at high temperatures so they will often be found in 20Cr-25Ni-Nb after solution treating and quenching [11].

Silicon – helps to enhance oxidation resistance but when the concentration is over 0.7 wt%, potential spalling of the oxide layer can occur [8].

Carbon and Nitrogen – They are generally found in the interstitial sites of the iron lattice, they contribute to the strength of the material by forming precipitates that assist in precipitate strengthening of the material. The content of carbon, however, is generally made to be quite low for high temperature stainless steels because the carbon will form chromium rich precipitates on the grain boundaries leading to chromium depletion from solid solution causing the corrosion resistance of the alloy to decrease on the grain boundaries. High carbon content also contributes to poor weldability [10]. Nitrogen, similar to carbon, assists in strengthening the material by forming nitrides like NbN and TiN. However, high nitrogen content was shown to lead to intergranular stress corrosion cracking in austenitic stainless steels like 304 [14]. Figure 1.3 shows the effect of increasing nitrogen concentration on the flow stress of an austenitic Nb-microalloyed steel [15].

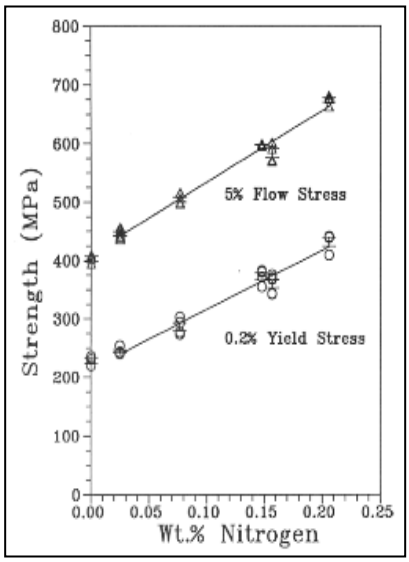

Figure 1.3. Strength as a function of nitrogen in steels [8, 15]

The 300 series including type 304, an 18Cr-8Ni stainless steel, is a common series of stainless steels that is used for a wide variety of applications because of its good weldability, corrosion resistance, and strength. For higher temperatures 316 and 316L are typically used because they have better creep, high temperature strength and corrosion properties. They provide good pitting corrosion resistance at elevated temperatures.

20Cr-25Ni based stainless steels including Alloy 709 are being looked at for high temperature applications due to their superior creep resistance, high temperature strength, and corrosion resistance. Adding more Ni generally makes the alloy more expensive but it helps the high

temperature mechanical properties. The 20Cr-25Ni series of stainless steel might require more cost up-front but could save money down the road if the material can outlast the other materials. The increase in Cr and Ni makes the alloy more corrosion resistant and increases the high temperature mechanical properties. Using the other alloying elements to create fine MX precipitates have been very beneficial for optimizing the 20Cr-25Ni series of stainless steels.

1.4 Creep Mechanisms

1.4.1 Overview of Creep

Creep is defined as time-dependent plasticity generally tested under a constant stress or load, often below the yield stress of the material, with the temperature typically being over $0.5T_m$ (with T_m being the melting temperature). Some studies have shown creep at temperatures of $0.09\text{-}0.21T_m$ for certain alloys but generally for most materials creep begins to occur at $0.4\text{-}0.5T_m$ [16, 17, 3]. It typically takes several years for well-engineered structural components to be affected by creep. This process however, can be accelerated by increasing the temperature or applied stress to be able to see creep in shorter periods of time. This makes creep a primary concern for components at elevated temperatures for long periods of time.

There are generally three stages of creep that occur. They can easily be seen when plotting the plastic strain (ε_p) with the time (t) under constant load and temperature, shown in Figure 1.4. The first stage is known as the primary creep stage and is labeled "I" in Figure 1.4. In the primary creep region the strain rate or $\dot{\varepsilon} = d\varepsilon/dt$ is not constant. In this case the strain rate decreases as the time and strain increase. This is due to strain hardening or a decrease in free or mobile dislocations [3]. An inverse case of primary creep has been found for certain alloys that experience solute drag with "3 power creep" [17]. In the secondary stage (labeled II), also called the steady-state creep stage, where the strain rate is constant ($\dot{\varepsilon}_{ss}$) [17]. The steady state is often attributed to the rate of dislocations being created, causing hardening, is equal to the rate of recovery, causing softening. It is a manifestation of a dynamic balance between strain hardening and recovery. The tertiary creep (labeled III) or accelerated creep is when the microstructure evolves and damage evolution takes place.

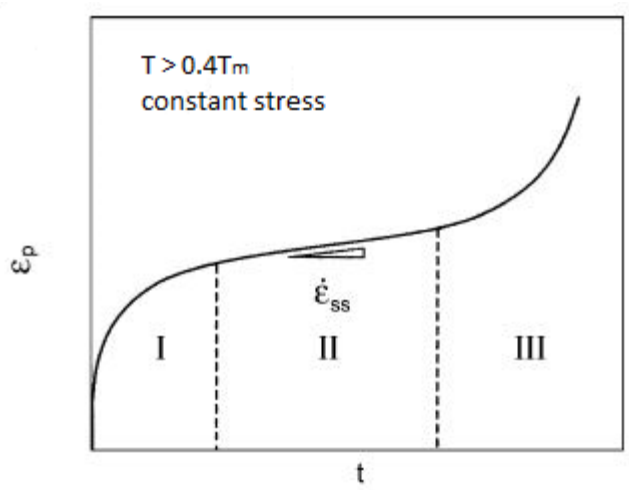

Figure 1.4. Typical creep curve under constant true-stress and temperature [17]

Microstructure evolution is usually dynamic recovery, dynamic recrystallization, coarsening of precipitates, or other phenomena. Damage evolution generally is caused by the formation of cracks and voids or cavities often on grain boundaries [3]. The testing conditions can cause a wide variety of creep curves with varying length of the primary, secondary and tertiary creep stages. Increasing the temperature and stress will result in more plastic strain over a period of time resulting in faster failure (Figure 1.5). Failure is typically the end of the creep curve.

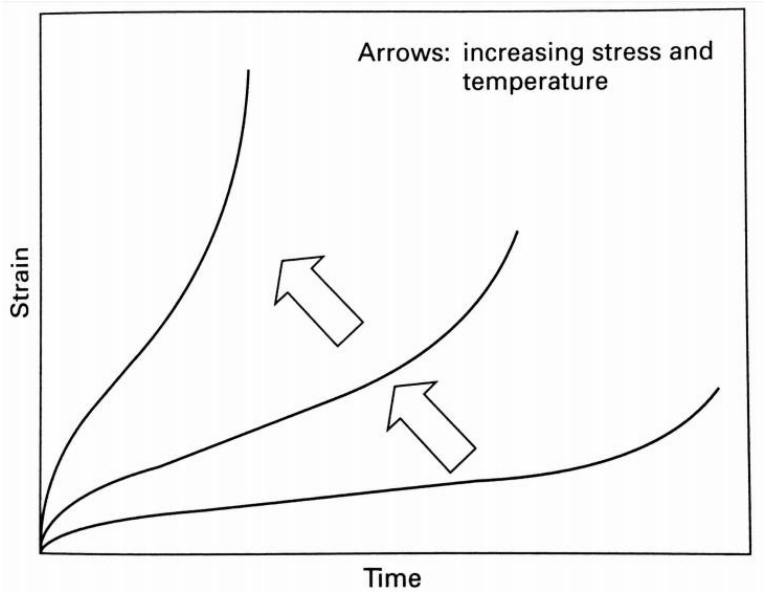

Figure 1.5. Schematic creep curves with increasing stress and temperature [3].

Some creep resistant steels and alloys under certain conditions do not have a clear steady state creep stage. In these instances the creep curve will start with primary creep and move directly into tertiary creep. When this occurs the minimum creep rate can be defined as the moment the hardening in the primary is equivalent to the softening of the tertiary [3]. Research has shown that the microstructure during creep is constantly evolving for many creep resistant steels and alloys. This has led to many engineers and researchers preferring the term minimum creep rate over steady state creep rate because there is no true dynamic microstructural equilibrium for many materials [3]. Figure 1.6(a) and (b) show the creep curve and creep rate vs. time curve for a modified 9Cr – 1Mo (Grade 91) steel [18].

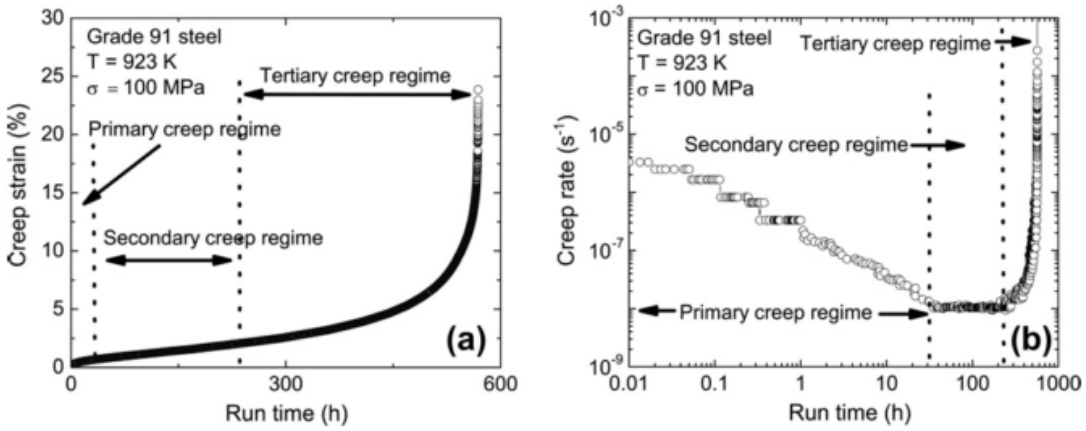

Figure 1.6. (a) A standard creep curve for Grade 91 steel, and (b) a creep rate vs. time showing the minimum creep rate being the same as the steady state creep rate [19]

A common equation to show the stress dependence of the minimum or steady state creep rate with the applied stress, is given by Norton's Law, Equation 1.1.

$$\dot{\varepsilon}_{\min \, or \, ss} = A\sigma^n \qquad (1.1)$$

$$A = A'\exp(-\frac{Q_c}{RT}) \qquad (1.2)$$

where $\dot{\varepsilon}_{min}$ or $\dot{\varepsilon}_{ss}$ is the minimum creep rate or steady state creep rate, respectively, σ is the applied stress, n is the stress exponent, A' is the parameter that includes grain size and test parameters, Q_c is the activation energy for creep, R is the universal gas constant, and T is the temperature in K [3]. The creep of materials can often be described by the Bird-Mukherjee-Dorn (BMD) equation.

$$\dot{\varepsilon} = A\frac{DEb}{kT}\left(\frac{\sigma}{E}\right)^n\left(\frac{b}{d}\right)^p \qquad (1.3)$$

where $\dot{\varepsilon}$ is the steady state strain rate, σ the applied stress, *d* the grain diameter, *A* the material dependent constant depending on the operating mechanism, *E* the elastic modulus, *b* the Burgers vector, *k* the Boltzmann's constant, *n* is the stress exponent, *p* is the inverse grain size exponent, and *D* the diffusivity which is described by the equation:

$$D = D_o exp(-Q/RT) \qquad (1.4)$$

where D_o is the pre-exponential constant also known as the frequency factor, *Q* the appropriate activation energy, *R* the universal gas constant, and *T* the temperature in K [8]. The BMD equation was found to be accurate for most high stress low temperature conditions. However, when the alloy is particle-hardened, the BMD equation tends to result in high activation energy and stress exponent. Ennis et al. studied the high stress exponents in comparison to the precipitates that act as dislocation barriers [10, 21]. In this type of situation, the findings are generally rationalized to find true creep mechanism of the alloy lead to the threshold stress being considered. This lead to the BMD equation to be modified for a precipitate hardened alloy. The additional stress added to the dislocations due to the precipitates is considered in the modified BMD Equation 1.5.

$$\frac{\dot{\varepsilon}_{ss}kT}{DEb} = A\left(\frac{\sigma-\sigma_{th}}{E}\right)^n\left(\frac{b}{d}\right)^p \qquad (1.5)$$

where σ_{th} is the threshold stress and all other terms have been previously defined. The threshold stress is the stress below which no creep deformation takes place. This makes the effective stress $(\sigma - \sigma_{th})$ what is actually contributing to creep deformation in the material instead of the applied stress [10]. This will provide a better understanding of the actual creep mechanism occurring in the material. The resultant stress exponent and activation energy are often used to determine the mechanism of creep occurring in the material.

Table 1.1. Parametric dependence of various diffusion-controlled deformation mechanisms [22]

Creep Type	***n***	***p***	***Q***
Nabarro-Herring	1	2	Q_L
Coble	1	3	Q_{GB}
Harper-Dorn	1	0	Q_L
Grain Boundary Sliding	2	2	Q_{GB}
Solute Drag (Viscous Glide) Dislocation Creep	3	0	Q_S
Dislocation Climb Creep	5	0	Q_L
Low Temperature Climb Creep	7	0	Q_C

where Q_L is lattice diffusion, Q_{GB} is grain boundary diffusion, Q_C is dislocation core diffusion, and Q_S is solute diffusion. These mechanisms will be discussed in more detail later in this chapter.

1.4.1 Dislocation Creep

For dislocation creep the movement of dislocations happens to be the rate-controlling mechanism [12]. There are two forms of dislocation creep, dislocation slip or glide and dislocation climb. Dislocations are line defects that move along the slip plane of the material, for FCC the slip plane is of type {111}. Additionally, dislocation movement requires the bonds between the atoms to break which requires high enough temperatures or stresses [23]. When the dislocations are moving in the matrix material, they are often gliding in the slip plane. The dislocation glide can be slowed by the presence of barriers in the material that prevent or slow the dislocations from moving. These barriers can be a variety of things, solute atoms, precipitates, grain boundaries or other dislocations. These strengthening mechanisms include solid solution strengthening, precipitation hardening, and grain boundary strengthening. The stress required to drive dislocation glide is on the order of one tenth the shear stress for most materials [23]. Figure 1.7 schematically shows the dislocation models of glide and climb.

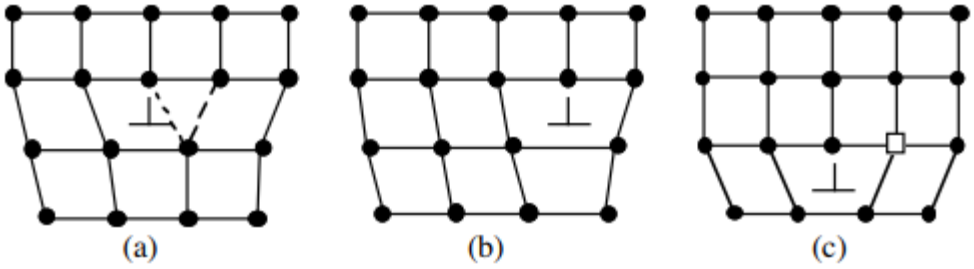

Figure 1.7. Dislocation glide (a) and (b) while (c) shows dislocation climb creating a vacancy.

When the dislocations meet with the barriers, they often cannot simply continue on the slip plane. Thus, the high temperatures will induce recovery of the pinned dislocations. As the material is strained more, the built up strain energy and high temperature can be enough to drive the recovery process. The recovery process decreases the dislocation density by allowing the dislocations to move into low energy arrays that are often subgrain boundaries. For this to occur there must be dislocation climb and slip which goes along with self-diffusion in the lattice [23]. At high homologous temperatures the dislocations are able to climb towards each other and mutually annihilate. This process is aided by vacancy diffusion [22]. For this reason it is often found that the activation energies for self-diffusion and creep are close to the same. As temperature increases, the atoms gain thermal energy and the vacancy concentration increases exponentially [23].

1.4.2 Grain-Boundary Sliding

The grain boundaries play an important role in creep deformation. Grain boundary sliding can occur at high temperatures which also can lead to the creation of vacancies [7]. The higher temperatures causes the grain boundaries to soften, allowing creep to occur through grain boundary sliding. Grain boundary sliding increases with temperature and grain boundary area. Where smaller grains significantly increase the grain boundary area so large grained materials are favored for creep resistance. At low temperatures grain boundaries prevent dislocation movement increasing the yield strength of the material, however at high temperatures they facilitate deformation by sliding [24]. The grain boundaries often act as a quasi-viscous material that flows at elevated temperatures.

1.4.3 Diffusion Creep

Diffusion creep is the creep mechanism that is caused by the flow of vacancies and interstitials through a crystal under the influence of applied stress causing grain boundary deformation. The diffusivity of a material increases with temperature which will lead to more deformation [7]. There are two major types of diffusion creep. As shown in Figure 1.8, the flow of vacancies through the grain boundaries is often called Coble creep, whereas The flow of vacancies through the grains is often called Nabarro-Herring creep. The vacancies migrate from grain boundaries in compression to grain boundaries in tension. The path the vacancies take, either through grain boundaries or through the grains, determines if it is Coble or Nabarro-Herring creep, respectively.

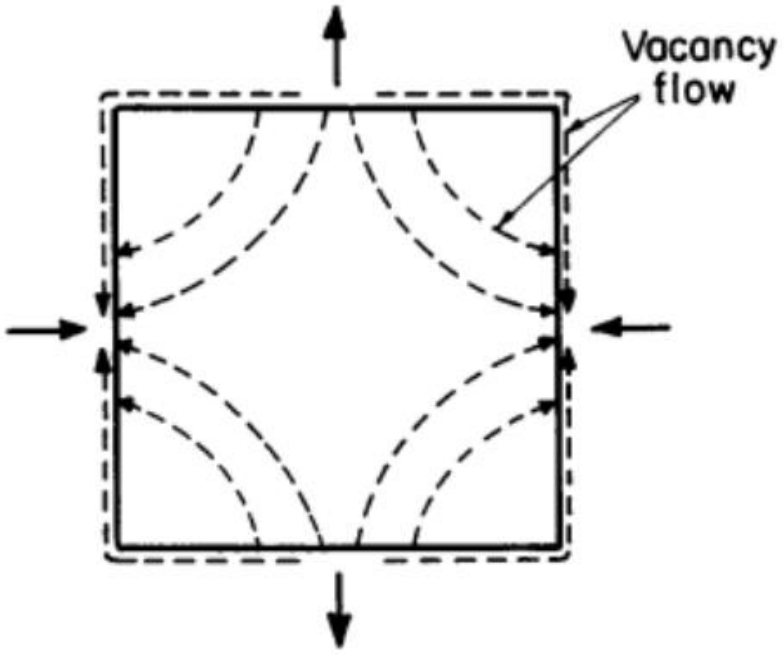

Figure 1.8. The principle of diffusion creep showing vacancy flow through the grains (Nabarro-Herring creep) and vacancy flow though the grain boundaries (Coble creep) [25]

1.5 Fatigue and Creep-Fatigue Crack Growth

Understanding fatigue crack growth (FCG) of materials is crucial for preventing failure of components. Cracks and defects are often present in fatigued components that still maintain their structural integrity. However if the crack grows, it could lead to catastrophic failures [26]. The impact of components that fail can have varying impacts. Low relative impacts could be

replacing a paper clip that failed due to fatigue, while high relative impacts can be the loss of millions of dollars in a plant downtime due to a critical component failing or in some cases the loss of human life. The DeHavilland Comet crash was a catastrophic FCG failure that killed 56 passengers. These events caused researchers to develop models for FCG and find ways to detect cracks and defects in components. One of the most widely used models for FCG was given by Paris et al., as shown below [27].

$$\frac{da}{dN} = C\Delta K^m \quad (1.6)$$

where *da/dN* is the crack growth rate, ΔK is the alternating stress intensity, *C* and *m* depend on material properties, microstructure, environment and other variables. This is often referred to as the Paris law. When ΔK and *da/dN* are plotted on a log/log plot, it fits a straight line and can be used to describe stage II of FCG, as shown in Figure 1.9.

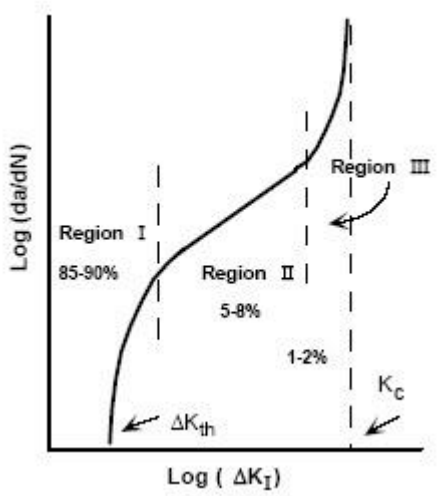

Figure 1.9. Illustration of the three stages of crack growth [28]

Well engineered components spend 90 percent of their lives in stage I. Stage I is also where the threshold can be determined which aids in understanding if a crack will even grow and is important for damage tolerance design [26, 29]. In stage III, the crack growth becomes unstable and often leads to rapid failure.

At high temperatures FCG is not the only concern; creep also contributes to crack growth. In nuclear/coal reactors, jet turbine engines, and other high temperature applications creep can cause crack growth in materials. Most of these components do not experience pure creep or

pure fatigue but likely experience a combination of the two. Creep-fatigue crack growth (CFCG) is crucial for understanding high temperature applications of materials to predict the life of components. The crack growth with time ($\dot{a}$) can be given in Equation 1.7 [30].

$$\dot{a} = \left(\frac{da}{dt}\right)_{cycle} + \left(\frac{da}{dt}\right)_{time} \qquad (1.7)$$

where $(da/dt)_{cycle}$ is the crack growth rate due to fatigue and $(da/dt)_{time}$ is the crack growth rate due to creep. This equation assumes that the crack growth due to creep and fatigue are independent of each other.

Nikbin, Smith and Webster [31, 32] developed a model (NSW model) for creep crack growth that uses a crack tip parameter *C**. The NSW model is most commonly used as a power law expression similar to the Paris law used for FCG [31]. The benefit of the crack tip parameter is that it allows data obtained in the laboratory to be applied to the actual structural behavior. This is because a crack with a certain crack tip will grow the same in the lab as it will in a structural component regardless of geometry and size [33].

1.6 References

[1] I. Charit and K. L. Murty, "Structural materials issues for the next generation fission reactors," JOM, vol. 62, no. 9. pp. 67–74, 2010.

[2] K. L. Murty and I. Charit, "Structural materials for Gen-IV nuclear reactors: Challenges and opportunities," J. Nucl. Mater., vol. 383, no. 1–2, pp. 189–195, 2008.

[3] F. Abe, T.-U. Kern, and R. Viswanathan, Creep-resistant steels, 1st ed. The Institute of Materials, Minerals, and Mining, 2008.

[4] OECD Nuclear Energy Agency, "Technology Roadmap Update for Generation IV Nuclear Energy Systems," Gen IV Int. Forum, pp. 1–66, 2014.

[5] IRSN, "Review of Generation IV Nuclear Energy Systems," 2015.

[6] T. Allen, J. Busby, M. Meyer, and D. Petti P, "Material challenges for nuclear systems," Materials Today, vol. 13, no. 12. pp. 15–23, 2010.

[7] M. Farooq, "Strengthening and degradation mechanisms in austenitic stainless steels at elevated temperature," Royal Institute of Technology, 2013.

[8] S. McCormick, "Effect of heat treatment and creep deformation on the microstructural characteristics of ATI 20-25+Nb austenitic stainless steel," University of Idaho, 2015.

[9] A. Gharehbaghi, “Precipitation Study in a High Temperature Austenitic Stainless Steel using Low Voltage Energy Dispersive X-ray Spectroscopy,” no. March, pp. 1–87, 2012.

[10] T. Shrestha, “Creep Deformation, Rupture Analysis, Heat Treatment and Residual Stress Measurement of Monolithic and Welded Grade 91 Steel for Power Plant,” University of Idaho, 2013.

[11] T. Sourmail and H. K. D. H. Bhadeshia, “Microstructural evolution in two variants of NF709 at 1023 and 1073 K,” Metall. Mater. Trans. A, vol. 36, no. 1, pp. 23–34, 2005.

[12] S. Abouzari, “Solid solution strengthening effect on creep strength of austenitic stainless steel,” Royal Institute of Technology, 2012.

[13] A. F. Padilha and P. R. Rios, “Decomposition of austenite in austenitic stainless steels,” ISIJ Int., vol. 42, no. 4, pp. 325–327, 2002.

[14] S. Roychowdhury, V. Kain, S. Neogy, D. Srivastava, G. K. Dey, and R. C. Prasad, “Understanding the effect of nitrogen in austenitic stainless steel on the intergranular stress corrosion crack growth rate in high temperature pure water,” Acta Mater., vol. 60, no. 2, pp. 610–621, 2012.

[15] G. Chen, W. Y. Yang, S. Z. Guo, and Z. Q. Sun, “Strain-induced precipitiaon of Nb(CN) during deformaiton of undercooled austenite in Nb-microalloyed HSLA steels,” in Materials Science Forum, vol. 475–479, Trans Tech Publications, 2005, pp. 105–108.

[16] L. A. Deibler, “Room temperature creep in metals and alloys,” no. September, 2014.

[17] M. E. Kassner, Fundamentals of Creep in Metals and Alloys, Second Edi. Elsevier Ltd., 2008.

[18] T. Shrestha, M. Basirat, I. Charit, G. P. Potirniche, K. K. Rink, and U. Sahaym, “Creep deformation mechanisms in modified 9Cr-1Mo steel,” J. Nucl. Mater., vol. 423, no. 1–3, pp. 110–119, 2012.

[19] T. Shrestha, M. Basirat, I. Charit, G. P. Potirniche, K. K. Rink, and U. Sahaym, “Creep deformation mechanisms in modified 9Cr-1Mo steel,” J. Nucl. Mater., vol. 423, no. 1–3, pp. 110–119, 2012.

[20] A. S. Alomari, N. Kumar, and K. L. Murty, “Investigation on Creep Mechanisms of Alloy 709,” ASME 2017 Nucl. Forum, p. V009T02A003, 2017.

[21] P. J. Ennis, A. Zielinska-Lipiec, O. Wachter, and A. Czyrska-Filemonowicz, “Microstructural stability and creep rupture strength of the martensitic steel P92 for advanced power plant,” Acta Mater., vol. 45, no. 12, pp. 4901–4907, 1997.

[22] I. Charit and K. L. Murty, “Creep behavior of niobium-modified zirconium alloys,” J. Nucl. Mater., vol. 374, no. 3, pp. 354–363, 2008.

[23] J. Pelleg, Creep in Ceramics, no. i. Springer International Publishing, 2017.

[24] S. L. Kakani and A. Kakani, Material science, vol. 1. New Age International Publishers, 2004.

[25] T. G. Langdon, "Creep at low stresses: An evaluation of diffusion creep and Harper-Dorn creep as viable creep mechanisms," Metall. Mater. Trans. A, vol. 33, no. 2, pp. 249–259, 2002.

[26] Albertson, T. (1996). *Fatigue crack growth behavior of two titanium alloys at room and elevated temperature*. University of Idaho.

[27] Paris PP, Erdogan FF. A Critical Analysis of Crack Propagation Laws. ASME. J. Basic Eng. 1963;85(4):528-533. doi:10.1115/1.3656900.

[28] "Application of Fracture Mechanics," Total Materia, 2011. [Online]. Available: https://www.totalmateria.com/page.aspx?ID=CheckArticle&site=kts&NM=353.

[29] R. I. Stephens, A. Fatemi, R. R. Stephens, and H. Fuchs, Metal Fatigue in Engineering, 2nd ed. 2001.

[30] Liu H, Bao R, Zhang J, Fei B. A creep–fatigue crack growth model containing temperature and interactive effects. International Journal of Fatigue. 2014; Vol. 59:34–42.

[31] Andrews, B. J. (2014). Creep-fatigue modelling in structural steels using empirical and constitutive creep methods implemented in a strip-yield model (Order No. 1571591). Available From Dissertations & Theses @ University of Idaho; ProQuest Dissertations & Theses Global.

[32] Webster GA, Ainsworth RA. High Temperature Component Life Assessment. Chapman & Hall, New York, 1994.

[33] Grover, P. S. (1996). Creep-fatigue crack growth in chromium-molybdenum-vanadium base material and weldments (Order No. 9636260). Available From ProQuest Dissertations & Theses Global.

Chapter 2. Creep Behavior of Alloy 709 at 700°C

Martin Taylor[1], Jose Ramirez, Indrajit Charit[1], Gabriel Potirniche[2], Robert Stephens[2], and Michael Glazoff[3]

[1] Department of Chemical & Materials Engineering, University of Idaho, ID 83844

[2] Department of Mechanical Engineering, University of Idaho, ID 83844

[3] Idaho National Laboratory, Idaho Falls, ID 83401

Abstract

Alloy 709 is a potential austenitic stainless steel for structural applications in sodium-cooled fast reactors. In this study, creep tests on Alloy 709 specimens were performed at a temperature of 700 °C under applied stresses in the range of 125 to 250 MPa. The alloy exhibited a brief primary, insignificant secondary and prolonged tertiary creep stages. A Norton stress exponent (*n*) of 5.9 was obtained from the creep plots. Microstructural analyses were carried out for both as-received and crept specimens using optical microscopy, electron backscattered diffraction, and transmission electron microscopy. The microstructures of the as-received and crept specimens were compared. Transgranular mode of fracture surfaces was observed by examining the creep-ruptured specimens using scanning electron microscopy. Based on the creep data and microstructural observations, possible creep deformation and failure mechanisms are elucidated.

2.1 Introduction

Austenitic stainless steels are considered cost-effective materials if they have commensurate high temperature oxidation and creep resistance for prolonged duration under service conditions [1, 2]. Alloy 709 is a potential candidate material for structural applications in advanced nuclear reactors, particularly for sodium-cooled fast reactors (SFR). The steel has been down-selected from a list of other high temperature steels because of its superior high temperature properties including elevated temperature oxidation/corrosion resistance, creep strength, sodium compatibility and weldability [3]. A number of creep-resistant austenitic steels have been developed by modifying compositions of the 18/8 austenitic stainless steels. In 1980's, the 20Cr-25Ni based austenitic steel was developed for its creep-resistance in fossil fired power plants [4]. However, Alloy 709 was originally developed by Nippon Steel (Tokyo, Japan), as NF709. This steel has a composition close to ATI 20+25Nb™. These steels contain Fe-20Cr-25Ni (wt%) base composition and the alloy composition is tailored in such a way that the

austenitic phase is stabilized. The austenitic phase (close packed structure) is generally considered better for creep resistance compared to BCC ferritic phase (more open structure). The high Ni content in Alloy 709 provides enhanced stability to the steel at elevated temperatures (albeit it makes the steel more expensive) whereas high Cr content provides excellent high temperature corrosion/oxidation resistance. There are only a limited number of creep studies available in open literature on the creep behavior of Alloy 709. While it is likely that components will need to serve at temperatures around 550^{o}C, it is important to understand the creep behavior of this material at different temperatures.

The aim of the present study is to report on the 700^{o}C short-term creep behavior of Alloy 709 and to understand the characteristic microstructural evolution that takes place during creep deformation using different characterization tools. An attempt is also made to compare the obtained creep data from Alloy 709 with those of other austenitic stainless steels and to understand plausible operative creep deformation mechanisms.

2.2 Material and Procedures

An Alloy 709 plate with dimensions of 101.6 mm × 228.6 mm × 20.3 mm was received from the Oak Ridge National Laboratory (ORNL). The prior history of the as-received plate included hot-processing (forged and rolled) and annealing at 1100°C, followed by water quenching. The chemical composition of the Alloy 709 plate is given in Table 2.1.

Table 2.1. Chemical composition of Alloy 709 (in wt%)

C	Mn	Si	P	S	Cr	Ni	Mo	N	Ti	Nb	B	Fe
0.067	0.90	0.40	<0.005	<0.001	19.80	25.09	1.50	0.15	<0.01	0.26	0.0043	Bal.

Figure 2.1 shows a schematic of the plate showing the three primary orthogonal directions (rolling direction, transverse direction and normal direction). Sections from the Alloy 709 plate were cut and mounted in acrylic. Standard metallographic procedures involving sequential grinding and polishing were carried out. The final polish was taken to a 0.3 μm surface finish using alumina paste. After thoroughly rinsing the surface of these samples, Vickers hardness testing was performed using a LECO LM-100 microhardness tester on all three distinct faces (RD-TD, ND-RD and ND-TD) with very similar results. Six indentations were taken for each orthogonal plane. Essentially, no difference was observed in the Vickers hardness number

(VHN) on the three orthogonal faces with VHN's of 177 ± 4 on the RD-TD, 179 ± 5 on the ND-RD plane, and 179 ± 4 on the ND-TD plane,

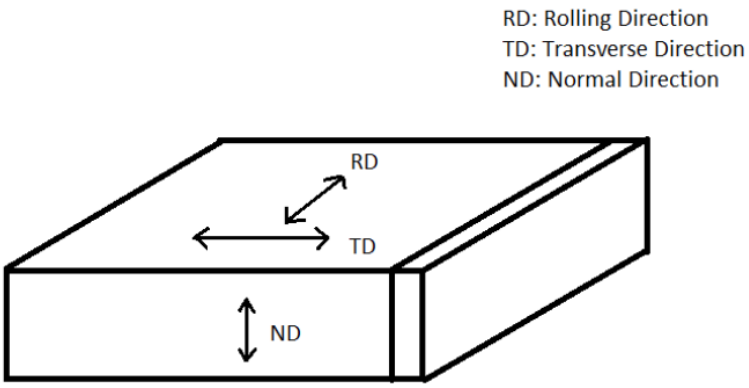

Figure 2.1. Schematic of the plate showing the rolling, transverse and the normal (thickness) directions.

The polished metallographic samples were then electrolytically etched with 10% (by mass) oxalic acid in deionized (DI) water at 6 V for 6-10 s, depending on the surface area of the specimen of interest [1]. Optical microscopy was conducted using an Olympus PMG-3 light microscope. The average grain size was determined from the metallographic images obtained using the mean linear intercept technique.

One section of the plate was machined into a round tensile specimen with a gauge length of 25.4 mm and a diameter of 6.53 mm. A tensile test was then performed at 700°C at a strain rate of 10^{-3} s^{-1} using an Instron 5982 Materials Testing System. Four sections were machined as round creep specimens with a gauge length of 25.4 mm and a diameter of 6.53 mm. Uniaxial constant-load creep tests were performed at 700 ± 1 °C with initial stresses ranging from 125 to 250 MPa using an Applied Test Systems 2335 lever arm (20:1) creep tester. Two Heidenhain ST-12 linear encoders measured the gauge elongation with an accuracy of ± 0.2 µm.

Samples were prepared for the transmission electron microscopy by grinding and polishing the samples until a thickness of approximately 100 µm thick or less was reached. Then a Gatan disc punch was used to obtain 3-mm diameter discs. Subsequently, electro-jet polishing on the disc samples were carried out using a Fischione Twin-Jet Polisher. A mixture of nitric acid (HNO_3) and methanol (CH_3OH) (1:9 ratio by vol.) was used as the electrolyte and the voltage used was around 30 V. Dry ice was used to keep the temperature of the electrolytic bath close to -40°C.

A JEOL 2010J transmission electron microscope (TEM) operated at an accelerating voltage of 200 kV was used to identify and study the characteristics of the second phase particles. Also, an energy dispersive spectroscopy (EDS) system attached to the TEM was used to carry out compositional analysis.

The polished metallographic samples were electro-etched and examined under a Zeiss Supra 35 Field Gun Emission Scanning Electron Microscope (FEG-SEM), revealing several of the precipitates and grain boundaries. Crept specimens were prepared either by sectioning along the loading direction exposing the grip and gauge sections, or cutting perpendicularly to the loading direction, exposing only the grip section. The specimens were then ground and polished down to 0.3 μm for SEM and EDS analyses. Vickers microhardness testing under 0.5 kgf load was carried out at several locations from the fracture tip to the grip region. At each location, six indentations were carried out.

Electron backscatter diffraction (EBSD) was obtained using the same sample preparation process listed above for the TEM samples except for the electro-jet polishing that was done for a shorter duration as a sample perforation is not required for EBSD. The surface- prepared disks were placed in the Zeiss Supra 35 FEG-SEM with the QUASOR^{TM} EBSD system. The sample stage was set at an angle of 70° with a working distance of about 16.5 mm. The SEM was operated at an accelerating voltage of 20 kV and put on high current mode. A binning of 8 pixel × 8 pixel was used in this study to obtain high enough resolution in the EBSD maps created.

ThermoCalc thermodynamic data can be passed on to the diffusion modeling software, DICTRA, and the data on the mobilities and driving forces from these two codes could be passed on to the microstructure evolution software, MICRESS. ThemoCalc was used in this work to determine what phases and precipitates are present at various temperatures and in what amount. The composition of Alloy 709 found in Table 2.1 was used for the ThermoCalc calculations.

2.3. Results and Discussion

2.3.1. Microstructural analysis of the as-received Alloy 709

A representative optical micrograph montage of the as-received Alloy 709 in all three orthogonal planes is shown in Figure 2.2. The microstructure consists of near equiaxed grains accompanied by a relatively high density of annealing twins. Grain sizes measured in all three

orthogonal planes did not exhibit any significant difference and the mean grain size is estimated to be 38 ± 3 μm. Figure 2.3a shows a TEM image of the as-received material showing presence of annealing twins. A representative EDS spectrum from one of the dark-contrast second phase particles is shown in Figure 2.3b. While the EDS showed the presence of Nb, the N content could not be identified unambiguously in the EDS spectrum despite a peak presence of N. In the literature, NbN is found to be fine stable particles. The dark-contrast particles noted in the same TEM image are most likely NbN given the size and EDS spectrum of the particles. The other particles that contain Nb in Alloy 709 are NbC or Z phase (CrNbN). However, Z phase particles are typically rod-shaped and found to be in detectable amount only in materials exposed to high temperatures for a long duration, not in a solution annealed material.

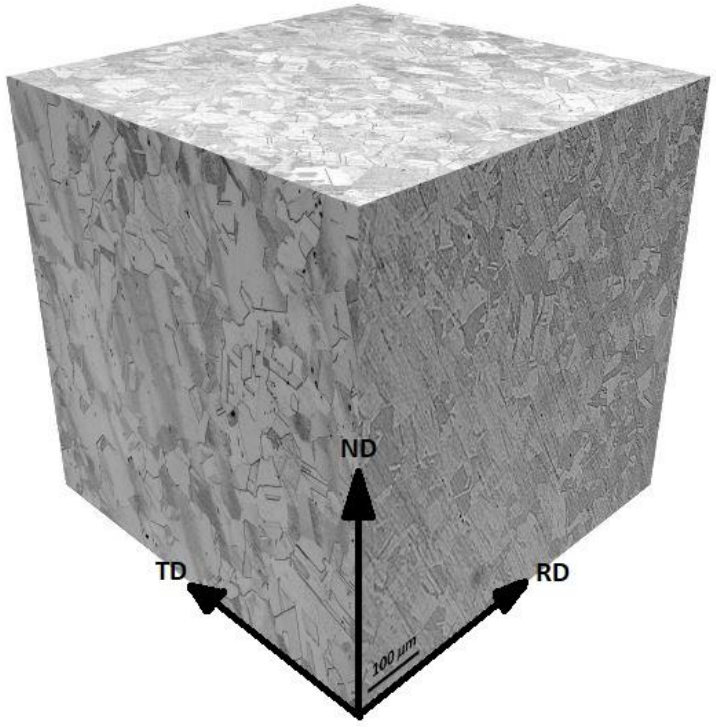

Figure 2.2. A three-dimensional representation of the optical micrographs in three orthogonal planes of the as-received Alloy 709 plate.

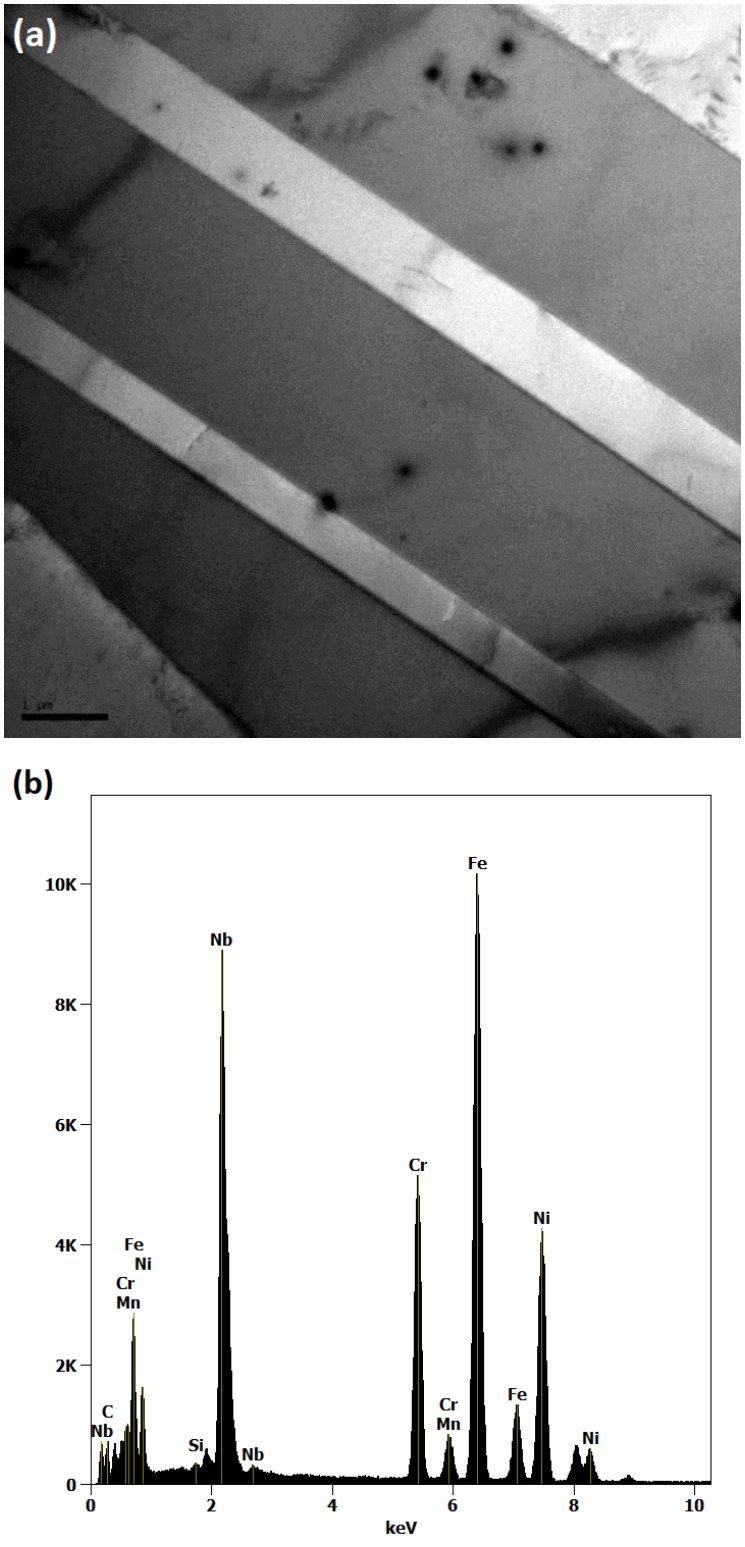

Figure 2.3. (a) A TEM bright field image of the as-received Alloy 709 showing annealing twins and dark-contrast globular second phase particles. (b) EDS spectrum of a dark particle.

2.3.2. Tensile behavior of the as-received Alloy 709 at 700°C

Tensile testing at 700°C was conducted to determine if the creep tests were performed at stresses around the yield strength. Two creep tests were conducted below the yield strength at 700°C and two tests at slightly above the yield strength in order obtain data in a reasonable period of time. The creep data will be reported in the next section. The true stress - true strain curve of Alloy 709 at 700°C at a strain rate of 10^{-3} s^{-1} (Figure 2.4). As common in austenitic stainless steels, the alloy exhibits a pronounced strain hardening regime. The stress-strain curve also exhibits slight indications of serrations right after yielding likely from dynamic strain aging (DSA). While DSA has largely been observed in mild steels as a result of interactions between mobile dislocations and interstitial impurities, it has also been observed in austenitic stainless steels like 316 SS where substitutional solutes modify such interactions. In 316 SS, it typically occurs at temperatures up to 600°C and strain rates in the range of 10^{-6} to 10^{-3} s^{-1} [5]. Alloy 709 exhibiting traces of DSA at 700°C is not unexpected as Alloy 709 is a more concentrated alloy with greater amounts of substitutional solutes being present in solid solution, such as Ni (10-14 wt% Ni in 316 SS as opposed to ~25 wt.% Ni in Alloy 709) leading sluggish diffusivity. Nevertheless, at lower temperatures (e.g. 600ºC) the DSA effect is expected to be more pronounced. Table 2.2 lists the measured engineering tensile properties (e.g. yield strength, ultimate tensile strength and the percentage elongation of failure) of Alloy 709 at 700°C. The large difference between the yield strength and ultimate tensile strength again confirms the significant extent of strain hardening.

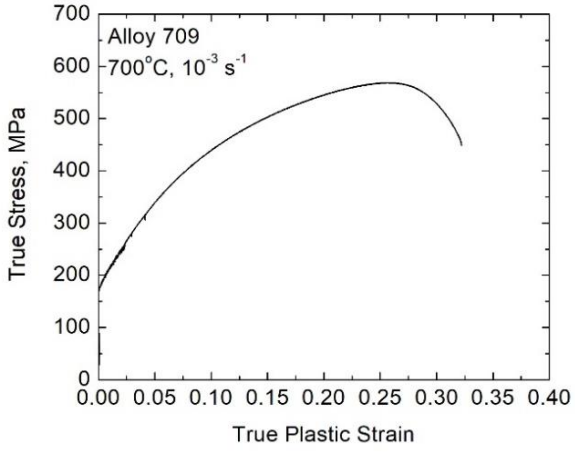

Figure 2.4. True stress - true strain curve for Alloy 709 at a temperature of 700°C and strain rate of 10-3 s-1

Table 2.2. Tensile properties of Alloy 709 at 700°C

Temperature	UTS (MPa)	YS (MPa)	Elongation
700 °C	449	178	46%

It is seen that the Alloy 709 maintained its yield strength at high temperatures making it attractive to structural applications under elevated temperatures. Other conventional austenitic stainless steels considered for structural applications in reactors have been found to have yield strengths below 178 MPa [6].

2.3.3. Creep tests at 700°C

2.3.3.1. Creep behavior of Alloy 709

The four accelerated creep tests were carried out on the as-received Alloy 709 specimens at 700°C. The corresponding creep curves are shown in Figure 2.5.a. The creep test at 125 MPa was performed up to 3,211 hours (without fracture) before unloading because of time constraint and the non-essentiality of the rupture life data for obtaining the Norton stress exponent. When initially loaded a small amount of instantaneous strain is created followed by a short primary and secondary stages, and a prolonged tertiary stage. As expected, the creep rate is found to rise with increasing applied stress from 125 MPa to 198 MPa. The higher stress tests were dominated by the tertiary creep zone. Figure 2.5.b shows the variation of creep rates as a function of time. The minimum creep rates are obtained from for each of the curves in Figure 2.5.b.

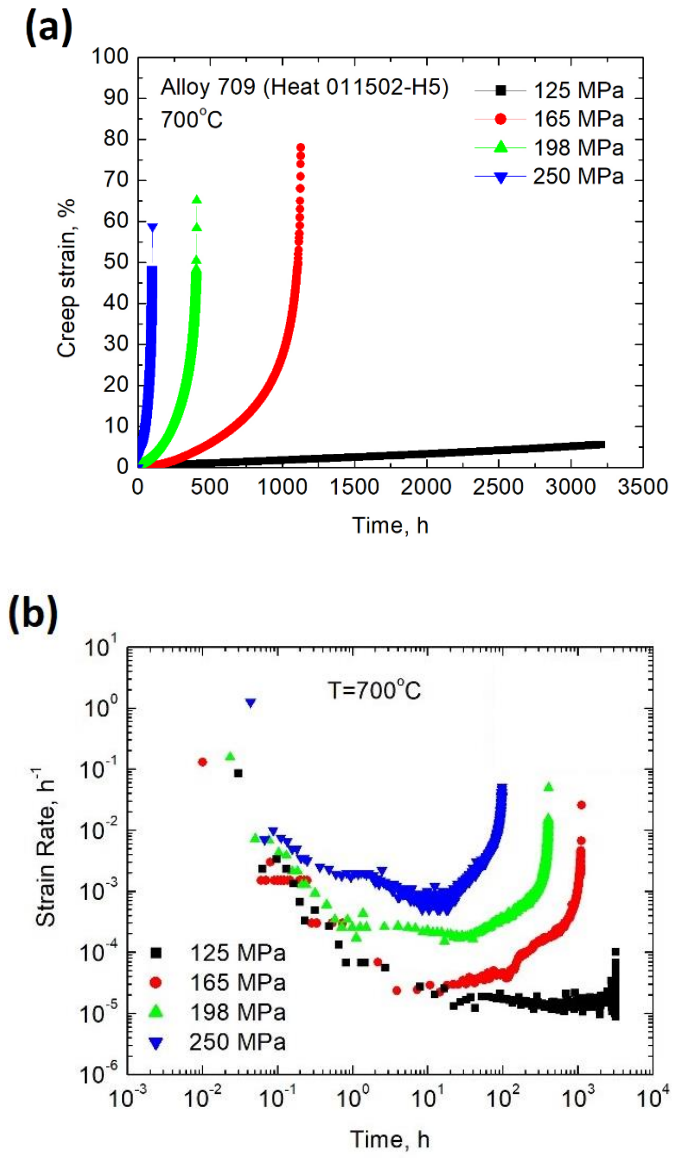

Figure 2.5. (a) Creep curves of the as-received Alloy 709 at 700°C under different applied stresses. (b) The corresponding variation of strain rate with time.

Table 2.3 shows the percentage elongation, percentage reduction in area and the minimum creep rates for the creep tests.

Table 2.3. Elongation, reduction in area, and minimum creep rate of Alloy 709 from various stresses at 700°C. (The symbol '*' means the sample did not rupture)

Applied Stress	**125 MPa**	**165 MPa**	**198 MPa**	**250 MPa**
% Elongation at Rupture	*	78%	65%	59%
%Reduction in Area	*	83%	81%	73%
Minimum Creep Rate, s^{-1}	4.17×10^{-9}	1.10×10^{-8}	6.10×10^{-8}	2.20×10^{-7}

The dependence of the minimum strain rate on the applied stress can be simply expressed by Norton's power law:

$$\dot{\varepsilon}_m = A\sigma^n, \quad (2.1)$$

where $\dot{\varepsilon}_m$ is the minimum creep rate, A is a material and temperature-dependent constant, σ is the applied stress, and n is the stress exponent). For this stress range and temperature, there was a single slope with an exponent of n = 5.9 from the double logarithmic plot of stress versus minimum creep rate as shown in Figure 2.6. This follows the experimental data obtained for NF709 steel from the datasheet. The stress exponent of 5.9 suggests that the creep mechanism at this temperature and stress range is most likely dislocation climb related. It is well known that a stress exponent between 4 and 7 indicates high temperature dislocation climb as the rate-controlling creep mechanism. However, because of the lack of additional data, it is not possible to unambiguously determine the creep mechanism at this point.

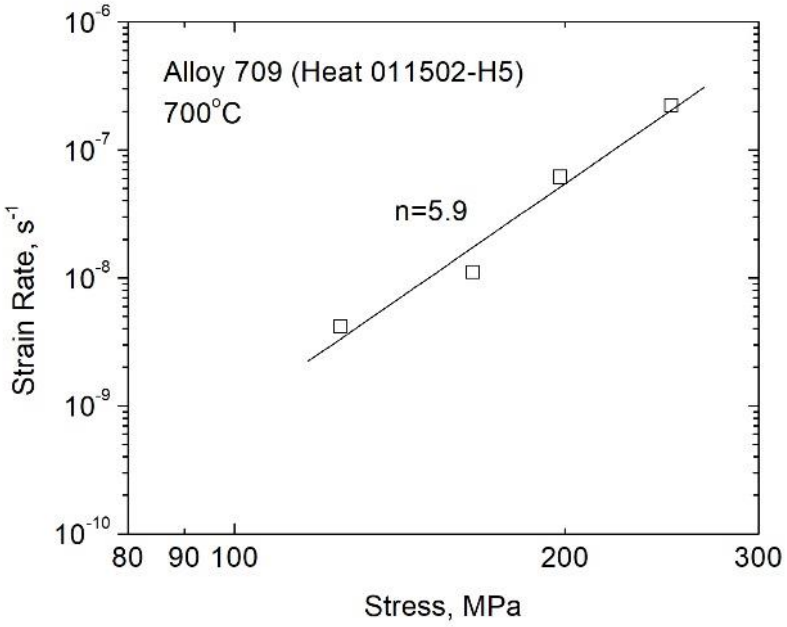

Figure 2.6. The variation of minimum creep rate as a function of stress for the as-received Alloy 709 at 700°C

Figure 2.7 shows the double logarithmic plot of minimum creep rate versus applied stress in Alloy 709 at 700 ºC. In the same plot, creep data of various 316 SS [7, 9] and 347 SS. Creep data from the NF709 datasheet from the Nippon Steel are also plotted as well as creep data of Alloy 709 obtained by Alomari et al. [10, 11] is also included. Also, some special austenitic stainless steels such as 15/15DS [8], 21Cr-32Ni [12] are also included. We note some difference between the creep data of the various 316 data; they lie rather all in the left side of the dashed line. We know that 316 steels are mainly based 16-18Cr—10-14Ni and 347 SS is based on 17-19Cr—9-13Ni. On the other hand, the creep data of Alloy 709, NF709 (Fe-20Cr-25Ni based composition) and 15/15DS data fall on the right side of the dashed line. In fact, the dashed line was constructed to delineate the difference between the creep strength of these alloys. It clearly shows that at least at 700 ºC Alloy 709 maintains creep strength better than 316, 347 or 21Cr-32Ni austenitic stainless steels. The 15/15DS grade of austenitic stainless steel is a double-stabilized SS, slightly better creep strength than other grades even though it is very close to that of Alloy 709 of our study. The data of Alomari et al. [11] cuts through the delineation line, which is not according to the overall trend. It is to note here that creep tests were done via stress-change experiments by Alomari and coworkers [11]. All the other studies conducted monotonic

single stress creep tests. They also commented that threshold stress imparted by the particles led to the higher stress exponent values.

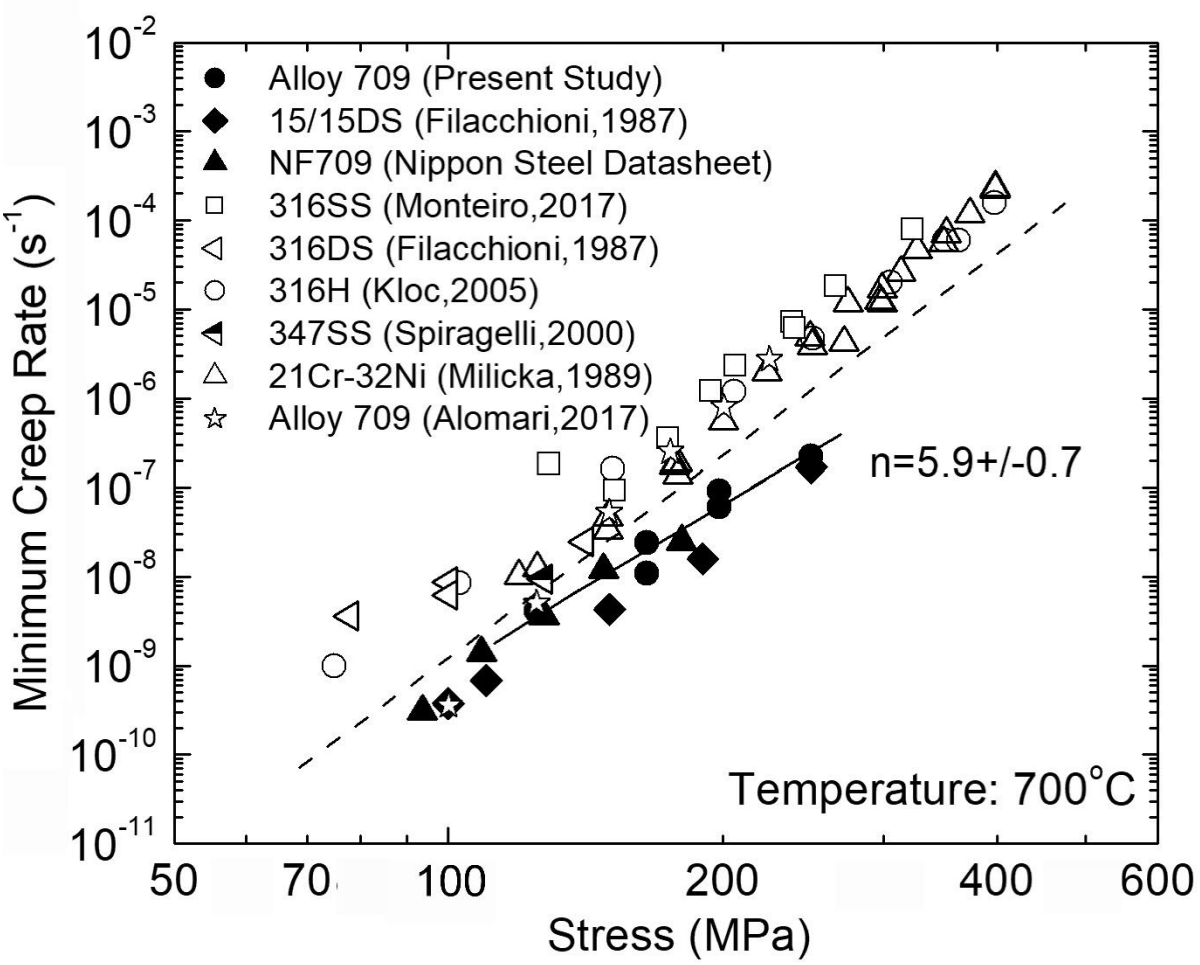

Figure 2.7. Comparison of minimum strain rates rate with applied stress at 700 °C for the as-received Alloy 709 at 700°C [7] - [13]

2.3.3.2. Fractography and optical metallography of creep ruptured specimens

Three of the tests (165, 198, and 250 MPa) were run up to rupture. A representative secondary electron SEM image of the specimen fracture surface tested at 700 ºC under an applied stress of 198 MPa is shown in Figure 2.8.a. Transgranular mode of fracture was observed in all fractured specimens with dimple-like features in the center (Figure 2.8.b) and shear lips around the edges (Figure 2.8.c). The dimples are likely the result of the coalescence of microvoids [3]. The fracture surfaces show mostly ductile fracture, which corresponds to the significant ductility observed in Alloy 709.

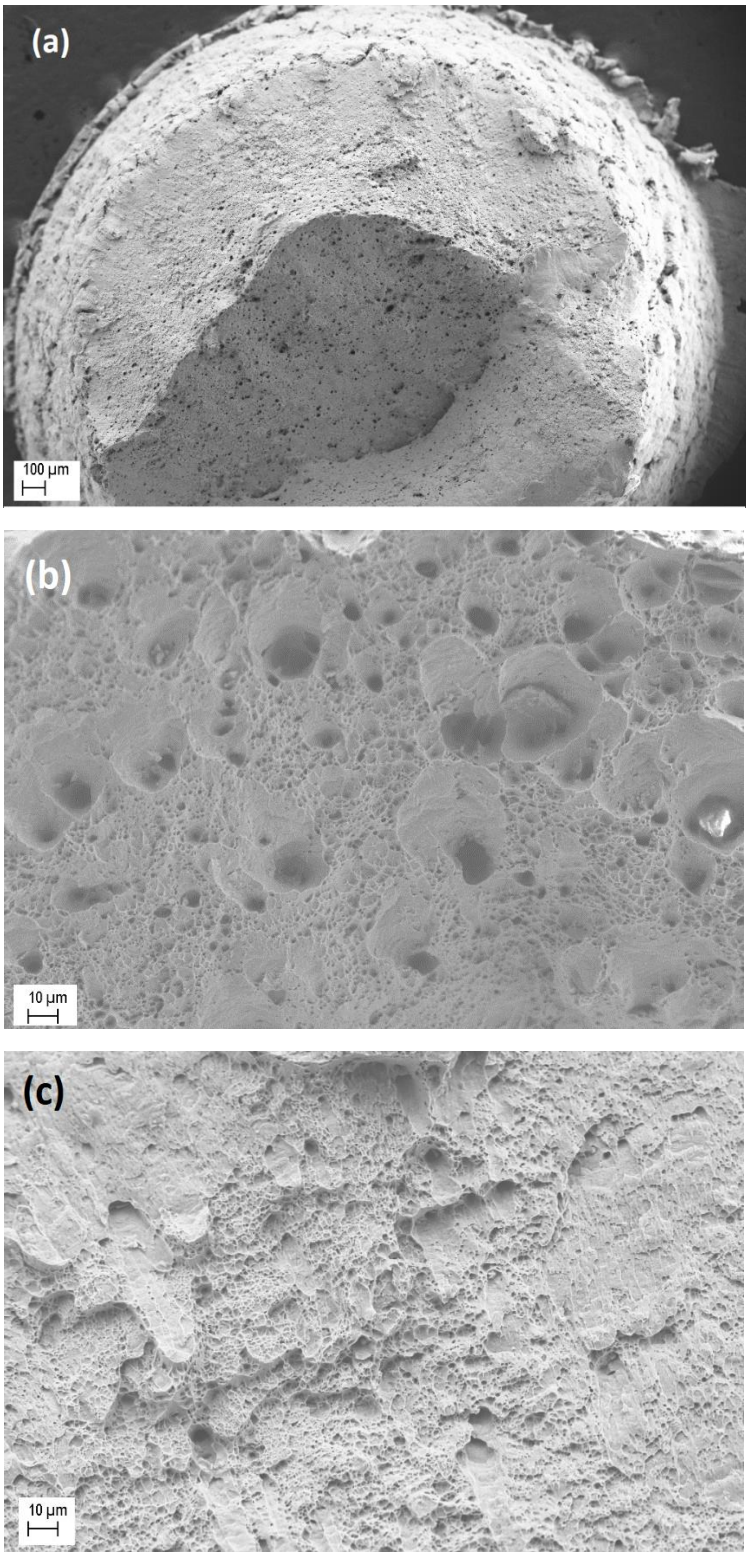

Figure 2.8. SEM images of the fracture surface of the crept Alloy 709 specimen tested under an applied stress of 165 MPa at 700°C: a) Ductile transgranular fracture with b) dimple-like features from microvoid coalescence and c) the presence of shear lip towards the outer edges.

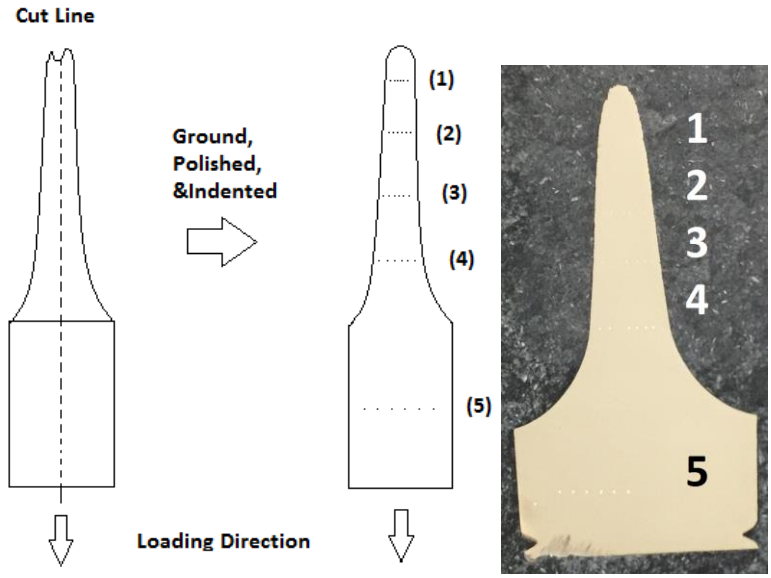

Figure 2.9. Schematic of the cut made on the crept specimen for hardness and microstructural analysis.

Six microindentations were taken to obtain average Vickers microhardness values at five different locations along the crept specimen section. Those microhardness values are listed in Table 2.4 along with the grain sizes measured from the corresponding optical micrographs.

Table 2.4. Vickers microhardness at the corresponding locations in Figure 2.9 for a crept Alloy 709 specimen (700 °C / 165 MPa)

Location Number	**Section**	**Local True Strain $\ln(A_o/A)$**	**Vickers Hardness Number (VHN)**	**Average Grain Size (μm)**
1	Gauge near fracture tip	1.4	246 ± 7	41.5
2	Gauge	0.9	230 ± 7	34.1
3	Gauge	0.6	219 ± 3	33.1
4	Gauge	0.2	211 ± 4	33.5
5	Grip	0	189 ± 8	34.0 (equiaxed)

After the microhardness values were obtained, the sample was polished again and electro-etched for optical microscopy and scanning electron microscopy (SEM). Optical microscopy revealed that the microhardness values increased with increasing grain size (Figure 2.10). The

grains were the largest near the tip of the creep-ruptured specimen, but did show elongation and decreased with the smallest average grain size in the grip section. This suggests that the Hall-Petch relationship is not the main contributing factor for the increase in hardness but could still have an influence because of the elongated grains and the formation of subgrains shown in Figure 2.12. The grains in the gauge section were elongated in the strain direction while the grains in the grip section were equiaxed. The loading direction for Figure 2.10 is in the horizontal direction. It is also observed that the density of twins decreased from the as-received material after being exposed to 700°C. Both grip and gauge of the crept specimen are found to be decorated by grain boundary precipitates with dark contrast. Note that these precipitates are not cavities. Zhao et al. [4] reported the microstructural characteristics of a creep-rupture test conducted on NF709 alloy at 650 ºC under an applied stress of 210 MPa for a total duration of 3,000 h. They also observed grain elongation along the applied stress direction and relatively equiaxed grains away from the fracture region similar to the present study. Furthermore, they also noted a hardness increase near the fracture region and the hardness falls while moving away from the gauge region toward the grip region.

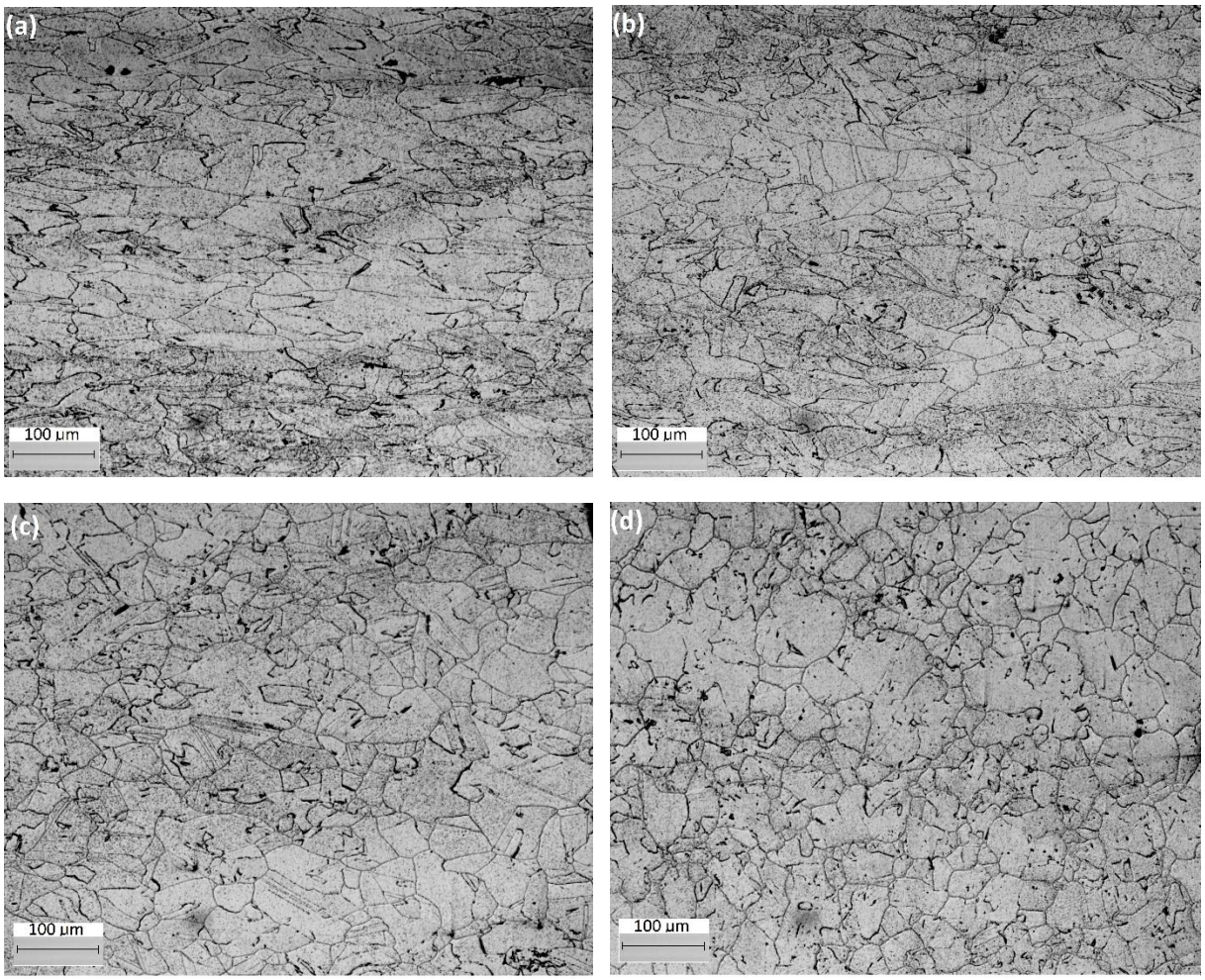

Figure 2.10. Optical micrographs of the crept Alloy 709 (700 °C / 165 MPa) specimen. (a) Corresponds to section 1 in Figure 2.9, (b) corresponds to section 2, (c) to section 3, and (d) to section 5 or the grip region.

2.3.3.3. Microstructural analysis of the crept specimen via EBSD and TEM

Both the grip and the gauge section of the crept (165 MPa / 700°C) specimen was cut perpendicularly to the loading direction and prepared for EBSD. The EBSD Euler maps as shown in Figure 2.11 revealed a more random variety of orientations in the grip section compared to the crept gauge section. On the other hand, the grains were more aligned (i.e. the overall orientation spread became narrower) as evidenced by similarly color-coded domains that are also smaller in size. EBSD data were also analyzed to create grain boundary orientation maps as shown in Figure 2.12 from the same grip and gauge regions of the crept specimen. The EBSD map of grip region shows only a few low angle grain boundaries (2-15^{o}) along with the high angle grain boundaries. Conversely, the EBSD grain boundary angle map in the gauge region shows the presence of several low angle boundaries (<15^{o}) formed in the gauge section

during creep deformation. The high density of these boundaries did not allow a good resolution of these boundaries. During creep, the whole specimen (including gauge and grip) was kept at about 700 ^{o}C for 1129 hours. The difference was that the gauge section experienced effects of both temperature and stress while the grip section saw only the effect of temperature, for the same time duration. The appearance of subgrain boundaries during creep deformation occurring via dislocation climb creep have been noted in several studies of other austenitic stainless steels [14]. The EBSD maps were taken of the ND-TD direction in which the loading direciton of the creep test were in the rolling direction.

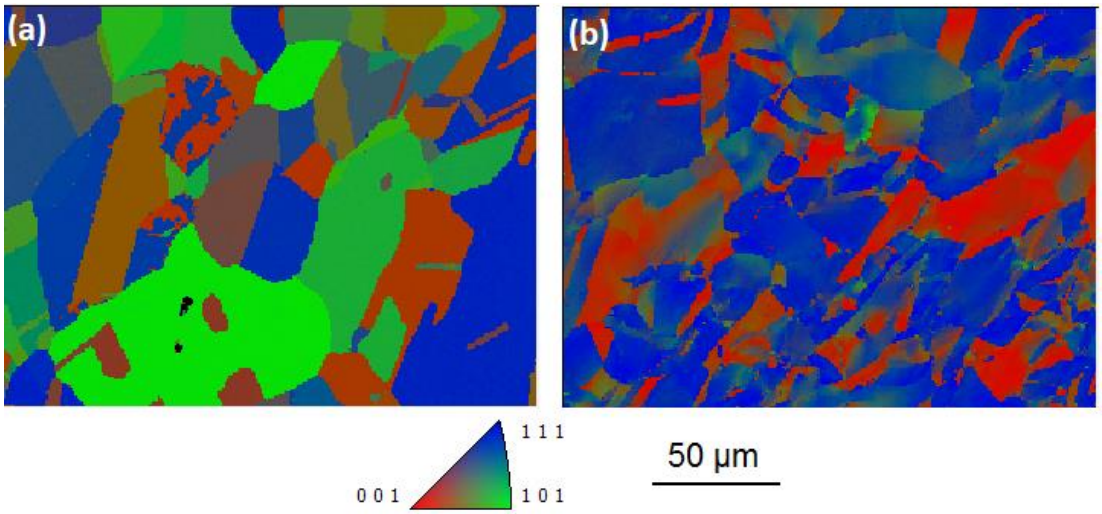

Figure 2.11. EBSD misorientation maps of the grip region (a) and gauge region (b) for the Alloy 709 specimen crept 165 MPa 700°C Alloy 709

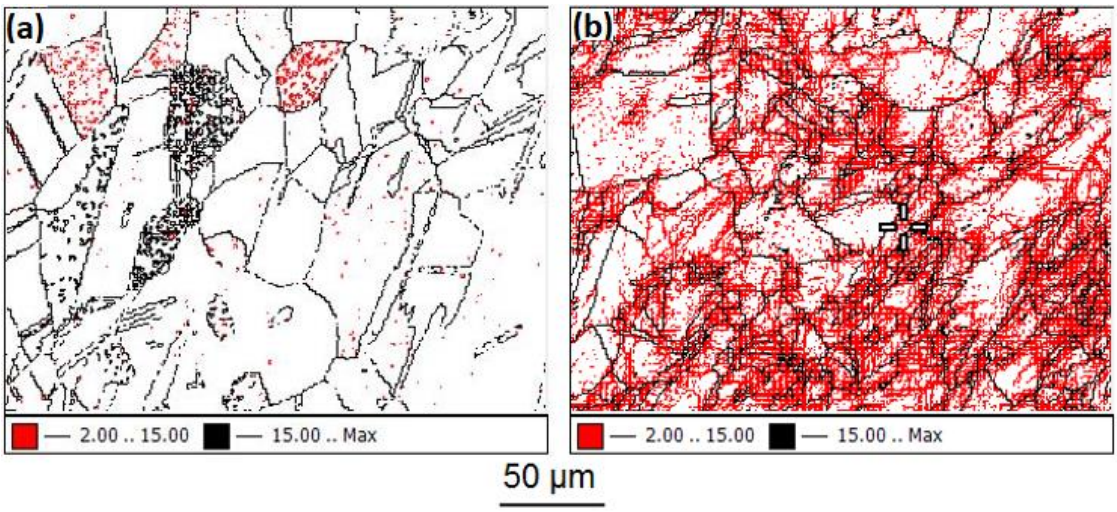

Figure 2.12. EBSD grain boundary angle maps of (a) the grip region and (b) the gauge region of the crept specimen (700°C / 165 MPa) of Alloy 709.

In order to further confirm these observations, TEM studies were performed on samples from both grip and gauge regions. Figure 2.13 (a) and (b) show bright field TEM images from the grip region of the crept sample. They do not show much activity of dislocations as can be expected of a statically annealed microstructure. In Figure 2.13 (b), one of the original twin boundaries in the microstructure could still be seen. However, in the gauge region as shown in Figure 2.14, the dislocation activity is quite evident. In both images 2.14 (a) and (b), formation of fine subgrains can be noted. It is important to recall that there was no such extensive formation of subgrains in the grip region of the crept specimen as well as the as-received Alloy 709 microstructure. The grain size of the Alloy 709 is in the range of 30-40 μm, the fine grain-like structures (0.5-1.0 μm) observed in the TEM image (Figure 2.14) are indeed subgrains. These subgrains were formed more or less throughout the crept microstructure. Thus, it can be confirmed that the subgrains seen as shown in Figure 2.14 (b) were created because of the creep deformation. Also, the EBSD study discussed in the previous section already confirmed the presence of a high proportion of low angle boundaries. As subgrains have most of their boundaries composed by low angle boundaries which are essentially of low angle nature, confirming the observed high proportion of low angle boundaries by EBSD study in the previous section. Although annealing twins were not the focus of this study, they were all but gone in the gauge section under creep as noted by TEM as well as EBSD studies.

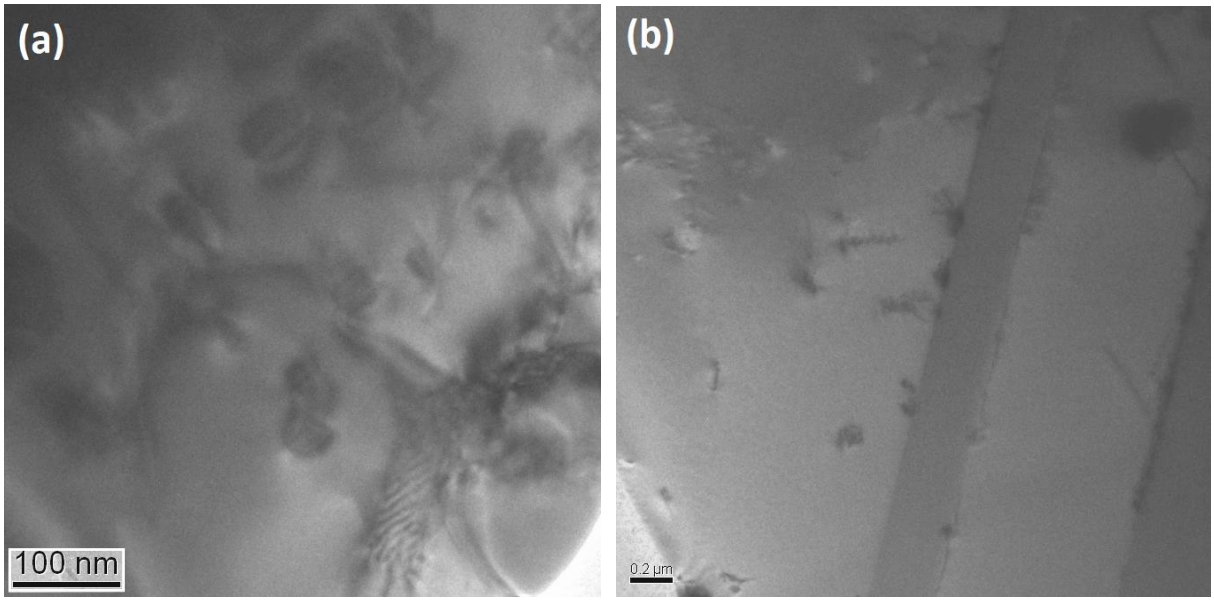

Figure 2.13. (a) and (b) Bright field TEM Image of the grip region of Alloy 709 crept at 700°C under an applied stress of 165 MPa

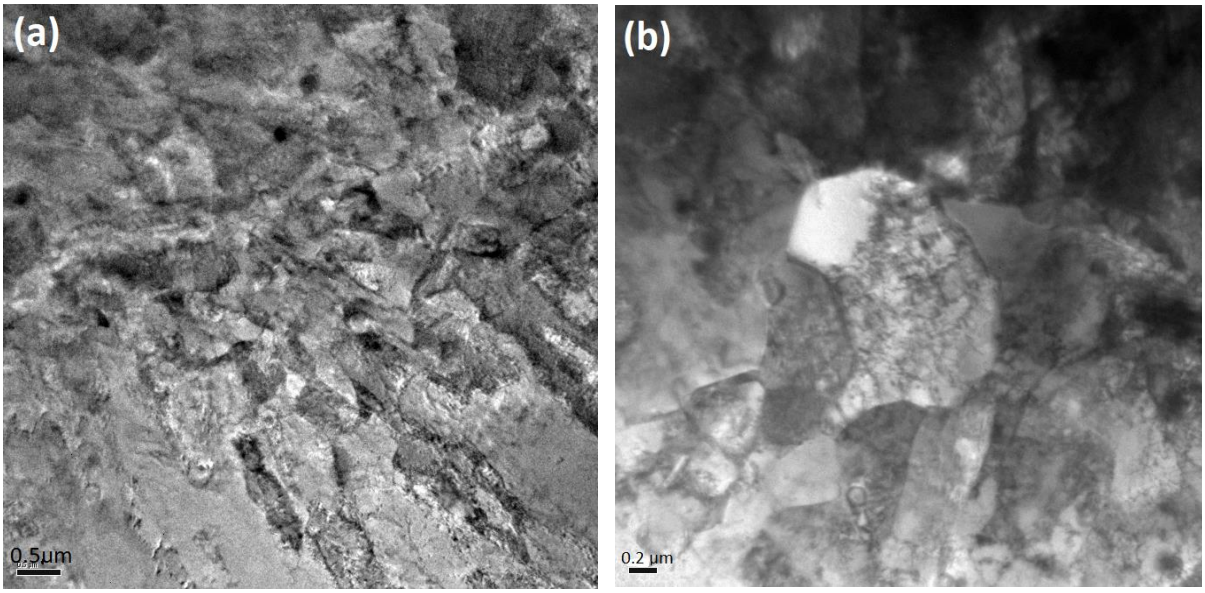

Figure 2.14. (a) and (b) Bright Field TEM images from the gauge section of Alloy 709 crept at a temperature of 700°C and an applied stress of 165 MPa.

The precipitates in the gauge region remained pretty stable, especially the MX type precipitates. No G phase could be detected even though Zhang *et al.* [4] reported the presence of G phase in the crept NF709. However, their creep test temperature was lower at 650 ^{o}C but at the same temperature. Some precipitates formed on the grain and twin boundaries. These precipitates are most likely $M_{23}C_6$ type given that the starting material was in the solution annealed (1100 ^{o}C) condition; upon high temperature exposure these precipitates started to form preferentially on the grain boundaries and to some extent on twin boundaries.

Thermo-Calc^{TM} calculations were used to predict the presence of various precipitates and their amounts (in mole fraction and volume fraction) in Alloy 709 as a function of temperature shown in Figure 2.15. At 550°C, it is expected to see $M_{23}C_6$, MX, Z phase, and σ phase while at 700°C the mole fraction of σ phase decreases significantly. The σ phase is known to be detrimental for creep properties. However, studies suggest it fully forms after longer aging times (2,500 to 6,000 hours) [1, 15]. Future creep studies will be done on aged Alloy 709 based on the Thermo-Calc^{TM} results along with thermokinetics results from TC-Prisma^{TM}.

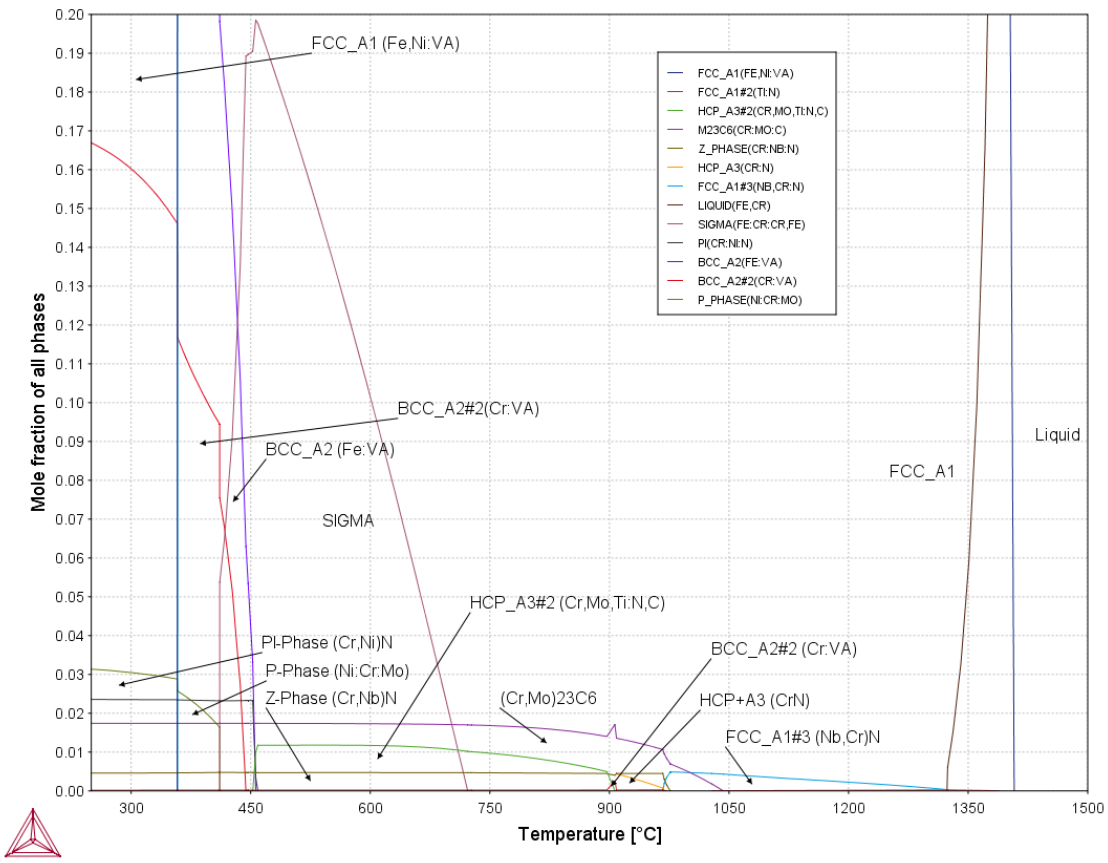

Figure 2.15. Thermo-Calc^{TM} results of Alloy 709 using the composition given in section 3

2.3.3.4. Relationship of substructural evolution and creep behavior

Subgrain formation is often found to accompany the traditional mechanisms such as recovery creep in the five power law creep regime [16]. During five-power creep new dislocations are generated and they rearrange themselves into low energy configurations because of long range stress fields between the dislocations. Additionally, the in-situ annihilation process where unlike dislocations get annihilated leaving dislocations of similar character left. These low energy configurations could be dislocation tangles, cell boundaries or subgrain boundaries. It has been determined from the TEM and EBSD studies that these low energy configurations of dislocation walls observed in the crept microstructure are essentially subgrain boundaries in the current study.

It is well established that the subgrain size is inversely related to the stress. Many studies developed a relation between the subgrain size (λ) and flow stress (σ) as shown in the following relation:

$$\lambda = \frac{BGb}{\sigma} \qquad (2.2)$$

where b is the Burger's vector, G is the shear modulus of the material and B is a material-specific constant that is approximately 10 for many materials. There is an empirical relation between the applied stress (σ) and subgrain size (λ) under the steady state creep as shown below [17]:

$$\lambda = 10b\left(\frac{\sigma}{G}\right)^{-1} \qquad (2.3)$$

At higher $\frac{\sigma}{G}$ values, the deformation mechanism changes causing the subgrian size dependence to change. However, this is not considered here as we could not discern any change in creep mechanism within the range of test conditions in the present study.

The magnitude of 'b' can be calculated from the lattice parameter (a) determined from the X-ray diffraction (XRD) pattern of the Alloy 709, assuming perfect dislocations of $a/2$ <110> type (Alloy 709 matrix having FCC lattice), the magnitude of 'b' is calculated. Then the elastic modulus (E) at 700 ^{o}C is taken as 148.9 GPa using material data sheet from Nippon Steel for NF709, and the shear modulus (G) is calculated using the following relation:

$$G = \frac{E}{2(1+\nu)} \qquad (2.4)$$

where ν is the Poisson ratio (here taken as 0.33).

Now inputting G as 57,270 MPa, b of 0.253 nm (as obtained in the appendix) and σ value (165 MPa) in Equation (2), the average subgrain size (λ) is calculated to be ~0.9 μm.

$$\lambda = \frac{10Gb}{\sigma} = \frac{10(57{,}270\ \text{MPa})(0.253\ nm)}{165\ \text{MPa}} = 0.878\ \text{nm} = \sim 0.9\ \mu\text{m}$$

Interestingly, the mean subgrain size measured from the TEM images of the crept specimen (700 ^{o}C / 165 MPa) was between 0.6 to 1 μm, which matches well with the predicted value from the above analysis. More microstructural examination of the other crept specimens may provide further information on the dependence of the subgrain size on the applied stress.

In the above analysis, the 'B' value is taken as 10. However, 'B' is a material-dependent constant and is found to vary depending on the stacking fault energy (SFE) with a smaller SFE

giving a smaller '*B*' value and vice-versa. However, further studies will be necessary to ascertain this variation.

2.4. Conclusion

The present work reported the results and analyses of a preliminary investigation of the creep behavior of Alloy 709 that is currently being considered for use as a structural material for the sodium fast reactor. The following observations and conclusions were made:

- At 700°C, Alloy 709 experienced slight dynamic strain aging with a yield strength of around 180 MPa and an ultimate tensile strength of about 450 MPa.
- Accelerated creep tests at 700 °C showed a brief primary, short secondary, and long tertiary zone.
- Norton plots of the creep tests resulted in a stress exponent of ~6, suggesting the most likely rate-controlling creep mechanism to be dislocation climb. However, further creep test data is needed to unambiguously determine the operating micro-mechanism.
- Ductile transgranular fracture surfaces were observed by SEM with dimple-like features from microvoid coalescence. However, the optical microscopy of the longitudinal cross-section did not reveal any cavitation or cracking away from the fracture tip, implying that most of the damage was concentrated in the immediate vicinity of the fracture tip.
- Although optical microscopy did not show subgrain formation, cross sectional results from the EBSD showed low angle grain boundaries (<15°) forming in the gauge section of the 700°C 165 MPa crept specimen. Orientation maps from the EBSD showed significant grain alignment in the gauge section compared to the grip section.
- TEM results confirms subgrain growth and also shows a decrease in precipitates in the gauge section compared to the grip.
- Thermo-Calc was used to find the phases present and will be used for future creep studies on aged Alloy 709.

2.5 References

[1] T. Sourmail and H. K. D. H. Bhadeshia, "Microstructural evolution in two variants of NF709 at 1023 and 1073 K," Metall. Mater. Trans. A, vol. 36, no. 1, pp. 23–34, 2005.

[2] P. J. Maziasz et al., "Improved creep-resistance of austenitic stainless steel for compact gas turbine recuperators," Mater. High Temp., vol. 16, no. 4, pp. 207–212, 1999.

[3] E. Isaac Samuel, B. K. Choudhary, D. P. Rao Palaparti, and M. D. Mathew, “Creep deformation and rupture behaviour of P92 steel at 923 K,” Procedia Eng., vol. 55, pp. 64–69, 2013.

[4] Y. Zhao, J. Zhao, and X. Li, “Microstructural evolution and change in hardness during creep of NF709 austenitic stainless steel,” Acta Metall. Sin. (English Lett., vol. 24, no. 3, pp. 220–224, 2011.

[5] M. Ivanchenko, “Dynamic Strain Aging of Austenitic Stainless Steels and Ni Base Alloys,” AAlto University, 2010.

[6] S. Sham, “Advanced Reactor Concepts Program ARC Materials Development - Accomplishments and Plans,” 2013.

[7] G. Filacchioni, “Tensile and creep behavior of a new family of austenitic alloys: the double stabalized stainless steels,” Mater. Nucl. React. core Appl., vol. 1, pp. 191–198, 1987.

[8] “Nippon steel material data sheet NF709,” Nippon STEEL SUMITOMO Met. Corp., pp. 10–12, 2013.

[9] S. Monteiro Neves, F. Santos, W. Anacleto, and L. Paulo, “Creep Parameters and Dislocation Substructure in AISI 316 Austenitic Stainless Steel From 600oC to 800oC,” Mater. Res., no. 1, pp. 1–5, 2017.

[10] L. Kloc and J. Fiala, “Viscous creep in metals at intermediate temperatures,” Kov. Mater, vol. 43, no. 2, pp. 105 – 112, 2005.

[11] S. Spiragelli, “Constitutive equation for recovery controlled creep in the austenitic stainless steel X6 CrNiNb 18 11,” La Metall. Ital., vol. 88, no. 8, pp. 530–535, 1996.

[12] K. Milicka, “Dislocation creep of austenitic stainless steels Part 1. Stress and temperature dependences of steady state creep,” Acta Tech., vol. 34, no. 3, pp. 300–318, 1989.

[13] A. S. Alomari, N. Kumar, and K. L. Murty, “Investigation on Creep Mechanisms of Alloy 709,” ASME 2017 Nucl. Forum, p. V009T02A003, 2017.

[14] R. Zauter, F. Petry, H.-J. Christ, and H. Mughrabi, “High temperature creep behaviour and microstructure development of AISI 304L stainless steel,” *Mater. Sci. Eng. A*, vol. 124, no. 2, pp. 125–132, 1990.

[15] C.-C. Hsieh and W. Wu, “Overview of Intermetallic Sigma Phase Precipitation in Stainless Steels,” ISRN Metall., vol. 2012, no. 4, pp. 1–16, 2012.

[16] M. E. Kassner, Fundamentals of Creep in Metals and Alloys Five-Power-Law Creep, Second Edi. Elsevier Ltd., 2008.

[17] O. D. Sherby, R. H. Klundt, and A. K. Miller, “Flow stress, subgrain size and subgrain stability at elevated temperature,” Metal. Trans., vol. 8A, pp. 843–850, 1977.

Chapter 3. Constitutive Equation of Alloy 709

Martin Taylor[1], Indrajit Charit[1], Gabriel Potirniche[2], and Robert Stephens[2]

[1] Department of Chemical & Materials Engineering, University of Idaho, ID 83844

[2] Department of Mechanical Engineering, University of Idaho, ID 83844

Abstract

Alloy 709 is a 20Cr-25Ni austenitic stainless steel that is being considered for structural applications in sodium-cooled fast reactors. In this study, creep tests on Alloy 709 specimens were performed at temperatures of 600 °C and 700 °C under applied stresses in the range of 125 to 250 MPa. Additional creep tests were performed on thermally aged #1 sample (at 650 °C for 3 months) of Alloy 709. A stress exponent (*n*) of 6.7 was found for the tests performed at 600 °C, 5.9 at 700 °C, and 7.6 on the aged #1 crept at 700 °C was obtained from the Norton plots. The stress exponents found are within the range of 5-7 for the dislocation climb creep mechanism, so the threshold stress approach was not necessary to analyze the results. The creep behavior of Alloy 709 was described by the Bird-Mukherjee Dorn equation. Microstructural analyses were carried out for both as-received and crept specimens using optical microscopy, electron backscattered diffraction, and transmission electron microscopy.

3.1 Introduction

Austenitic stainless steels are considered cost-effective materials if they have adequate high temperature oxidation and creep resistance for prolonged duration under service conditions [1]. Alloy 709 is a potential candidate material for structural applications in advanced nuclear reactors, particularly for sodium-cooled fast reactors (SFR). The steel has been down-selected from a list of other high temperature steels because of its superior high temperature properties including elevated temperature oxidation/corrosion resistance, creep strength, sodium compatibility and weldability [1]. A number of creep-resistant austenitic steels have been developed by modifying compositions of the 18/8 austenitic stainless steels. In 1980's, the 20Cr-25Ni based austenitic steel was developed for its creep-resistance in fossil fired power plants [2]. However, Alloy 709 was originally developed by Nippon Steel (Tokyo, Japan), as NF709. This steel has a composition close to ATI 20+25Nb™. These steels are based on the Fe-20Cr-25Ni (wt%) composition, and the alloy composition is tailored in such a way that the austenitic phase is stabilized. The austenitic phase (close packed structure) is generally considered better for creep resistance compared to BCC ferritic phase (more open structure).

The high Ni in Alloy 709 content provides enhanced stability to the steel at elevated temperatures (albeit it makes the steel more expensive) whereas high Cr content provides excellent high temperature corrosion/oxidation resistance. There are only a few creep studies available in the open literature [3, 4]. While it is likely that components will need to serve at temperatures around 550 °C, it is important to understand the creep behavior of this material at different temperatures. However, fundamental information on the creep behavior of the alloy is still sparse.

In this study the microstructure of as-received and thermally aged Alloy 709 will be studied. Several creep tests on Alloy 709 at 600 and 700 °C will be considered in determining the creep mechanism of Alloy 709. The creep behavior is mainly studied by using the Bird-Mukherjee-Dorn (BMD) relation. Aged Alloy 709 was also crept at 700 °C and the minimum creep rates are used to compare the results with those of the as-received Alloy 709 and 316SS results.

3.2. Experimental

3.1.1. Material

Three plates of Alloy 709 were used in this study and the chemical composition is shown in Table 3.1. The plates #1 and #2 were hot-processed (forged + rolled) and annealed at 1100 °C, followed by water quenching. The third plate had an argon-oxygen-decarburization (AOD) melt condition, then was hot-rolled and solution annealed at 1100 °C. It was then water jet cut to remove heat affected zones. The first two plates were then machined into creep specimens with a gauge length of 2.54 cm and a diameter of 0.635 cm. The third plate was sectioned into 1.52 × 1.52 × 10.16 cm sections, then placed in the furnace for a thermal aging of 3 months at 650°C. Post-aging, it was further machined into creep round specimens shown in Figure 3.1.

Table 3.1. The chemical composition of the three plates of Alloy 709

Element	Plate #1	Plate #2	Plate #3
S	<0.001	0.0006	
C	0.063	0.078	0.07
Mn	0.88	0.9	0.91
Si	0.28	0.39	0.44
P	<0.005	<0.005	0.014
Cr	19.69	19.89	19.93
Ni	25	25.01	24.98
Mo	1.46	1.51	1.51
N	0.14	0.14	0.148
Nb	0.23	0.25	0.26
Ti	<0.01	<0.01	0.04
Cu			0.06
Co			0.02
Al			0.02
B	0.0022	0.0037	0.0045
Fe	52.2448	51.8183	51.5935

3.2.2. Microstructure characterization

Optical microscopy was performed on the as-received, aged #1, and crept sections of Alloy 709 specimens for the characterization of the grain structure. The samples were prepared by hot mounting, grinding and polishing to a 0.05 µm finish, and electro-etching for 6-15 s in 10% by mass oxalic acid. An Olympus PGM-3 light microscope with an attached digital camera was used to examine the microstructure and capture images.

More detailed images were captured using a Zeiss Supra 35 field emission gun scanning electron microscope (SEM) operated at an accelerating voltage of 10-15 kV primarily under secondary imaging mode. Energy dispersive spectroscopy (EDS) was used for identifying chemical compositions for precipitates and bulk material.

Further steps were taken to prepare samples for transmission electron microscopy (TEM) and electron backscatter diffraction (EBSD). The samples were ground and polished down to be less than 100 µm thick and were cut by a Gatan disk punch to obtain 3 mm disks. Then a Fischione twin-jet polisher was used to further reduce the thickness for TEM or remove the mechanical polishing layer for EBSD. A mixture of nitric acid (HNO_3) and methanol (CH_3OH)

(1:9 ratio by vol.) was used as the electrolyte and the voltage used was 30 V to 35 V. Dry ice was used to keep temperature of the electrolytic bath close to -40 °C.

A JEOL 2010J transmission electron microscope (TEM) operated at an accelerating voltage of 200 kV was used to identify and study the characteristics of the second phase particles. Also, energy dispersive spectroscopy (EDS) system attached to the TEM was used to carry out compositional analysis.

EBSD was obtained using the same sample preparation process listed above for the TEM samples except for the electro-jet polishing that was done for a shorter duration as a sample perforation is not required for EBSD. The surface- prepared disks were placed in the Zeiss Supra 35 FEG-SEM with the QUASOR^{TM} EBSD system. The sample stage was set at an angle of 70° with a working distance of about 16.5 mm. The SEM was operated at an accelerating voltage of 20 kV and put on high current mode. A binning of 4 pixel × 4 pixel was used in this study to obtain high enough resolution in the EBSD maps created.

3.2.3. Creep testing

Creep tests were performed at 600 °C and 700 °C with applied stresses between 125 and 250 MPa using an Applied Test System (ATS) lever arm (20:1) creep tester. The ATS creep testing system is shown in Figure 3.2. The furnace was set to alarm if there was more than a 1 °C offset. The LVDT used were two Heidenhain ST-12 linear encoders that measured the gauge elongation with an accuracy of ± 0.2 µm.

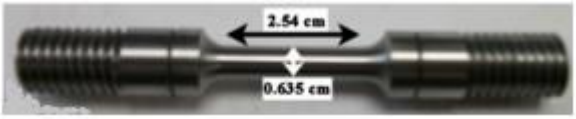

Figure 3.1. Creep test specimen geometry [5].

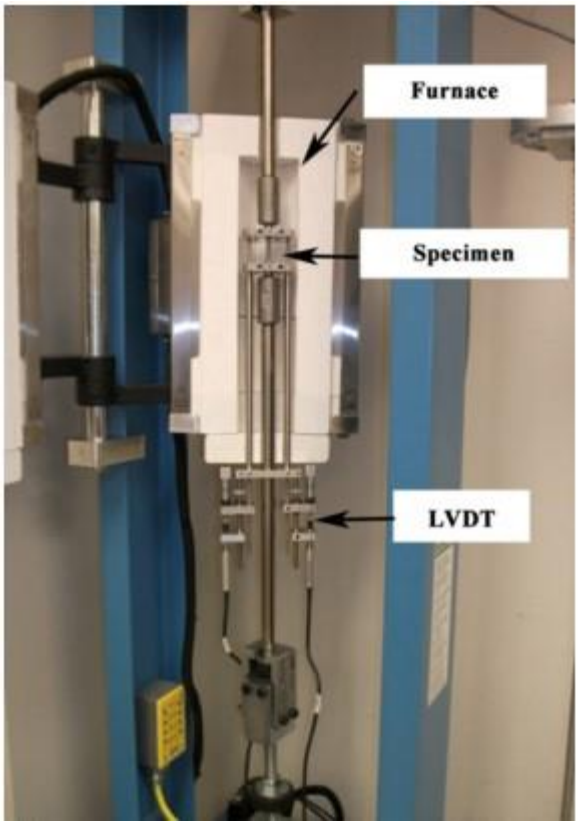

Figure 3.2. Uniaxial tensile creep tester with LVDT axial extensometer.

3.3. Results

3.3.1. Microstructural characteristics

The as-received microstructure of the bulk material is austenite (FCC) with grains sizes consistent on all three orthogonal planes that are 38 ±3 μm for the first plate and 37 ±2 μm for the second plate. The third plate had non-uniform grains with sections of larger grains similar to those found in the first two plates and other sections with much smaller grains. All three of the as-received plates showed the presence of twins.

For Alloy 709, one of the primary strengthening mechanisms comes from precipitation hardening. The as-received material for the first two plates has shown significant amounts of MX precipitates rich in Nb, as shown in Figure 3.3. These MX precipitates are beneficial for hardening the material and preventing dislocations from gliding under creep. M is typically Nb or Ti for Alloy 709 and X is N or C or (N, C) [6]. The specimens that were crept showed a significant increase of precipitate decorations on the grain boundaries.

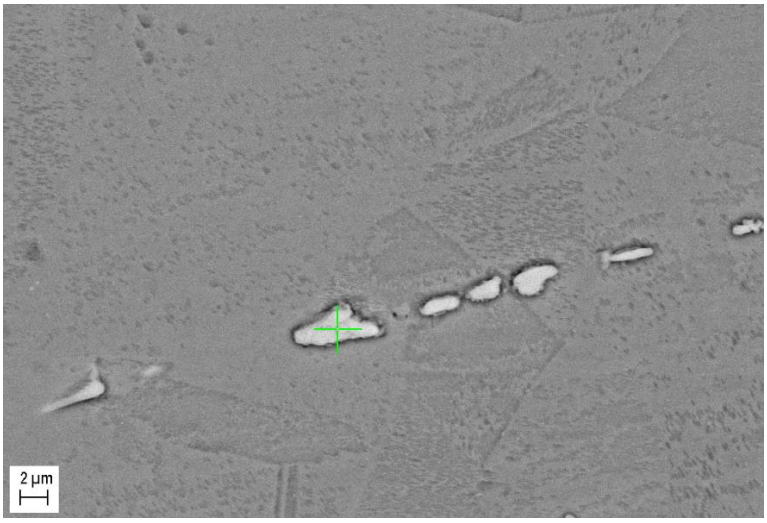

Figure 3.3. SEM SE image showing Nb rich MX precipitates found in the as-received Alloy 709

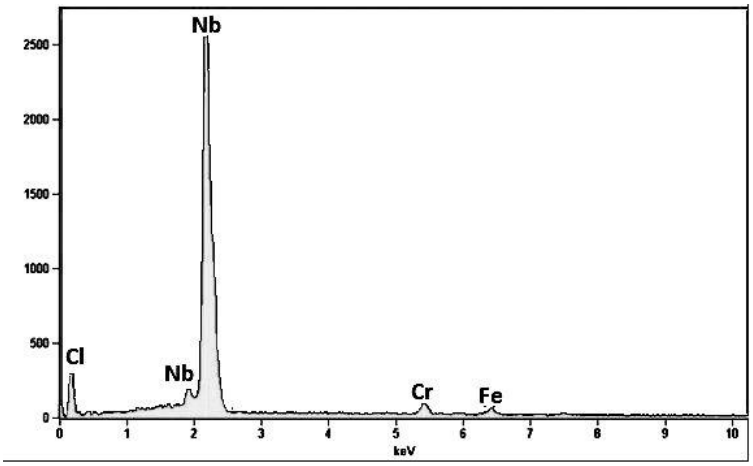

Figure 3.4. EDS spectra of the precipitate (plus marked) in Figure 3.3 showing a large Nb peak indicating it is a Nb rich MX precipitate.

$M_{23}C_6$ is a known precipitate that is often found on the grain boundaries in most stainless steels including NF709[6, 5]. For $M_{23}C_6$, the M typically stands for Cr but other elements like Fe and Mo can be present. In AISI 316 steel $M_{23}C_6$ has been found to have the form of $(Cr_{16}Fe_5Mo_2)C_6$ [7]. This precipitate composition depends heavily on the overall composition of the material and what is available (i.e., what is not already tied into a more stable precipitate). It is known that $M_{23}C_6$ phase dissolves at higher temperature. Given the original state of the as-received Alloy 709 was in solution annealed and quenched condition, $M_{23}C_6$ could not form in the as-received material. But as shown in Figure 3.5, thermally exposed grip part (i.e. without creep deformation) of a creep specimen did evolve to precipitate $M_{23}C_6$ carbide phases.

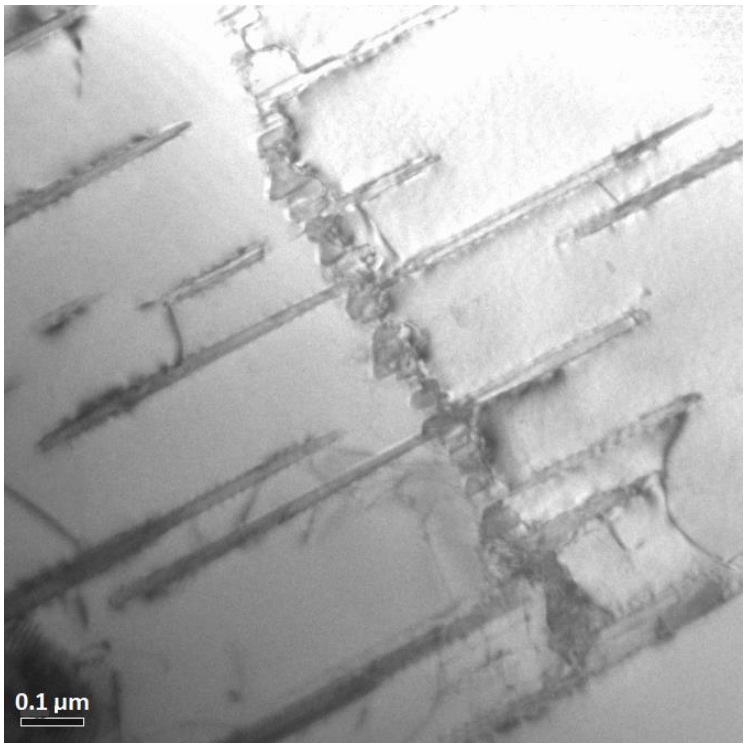

Figure 3.5. $M_{23}C_6$ plates form in the grip region of the 125 MPa crept specimen held at 700 °C for just under 3250 hr.

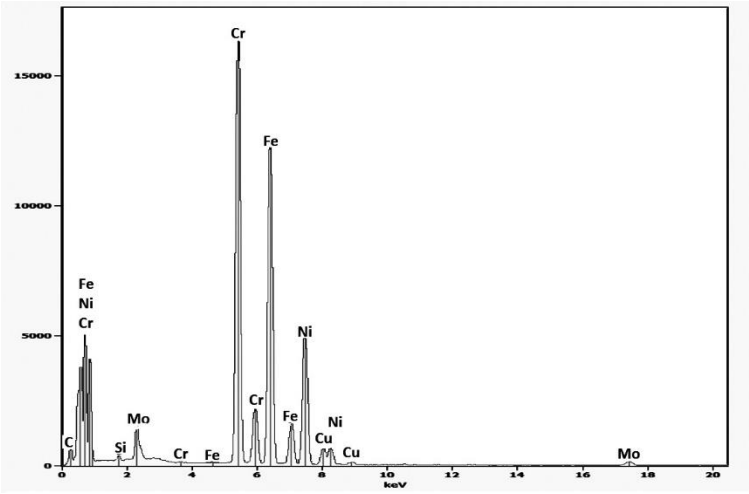

Figure 3.6. EDS spectra of the $M_{23}C_6$ plates shown above with high amounts of C, Cr, Fe, and Ni. Ni most likely present due to Ni in the matrix.

3.3.2 Creep properties

Creep is a time dependent plastic deformation that is generally observed at high homologous temperatures (0.4-0.5T_m or above). Alloy 709 is likely to reach temperatures where creep becomes a dominate mechanism of failure in SFRs. A typical creep curve of as-received

specimen of Alloy 709 tested at 700 °C and 165 MPa is shown in Figure 3.7 (a) with the corresponding variation of creep rate versus time shown in Figure 3.7 (b).

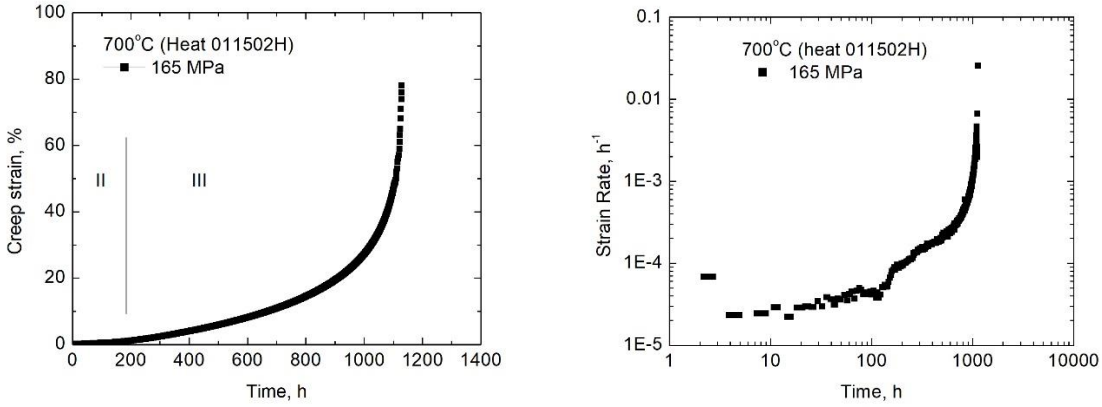

Figure 3.7. (a) Creep strain % with time showing no primary, short secondary (II) and an extended tertiary (III), (b) strain rate with time showing a minimum creep rate of around $4x10^{-5}$ h^{-1}.

The majority of the creep curves at 700 °C showed a very brief primary creep, insignificant secondary and an extended tertiary creep. However, this was no longer the case for stresses at or below 125 MPa at 700 °C or for the stresses applied at 600 °C.

3.4 Discussion

3.4.1 Bird-Mukherjee-Dorn Equation (BMD)

Thermally-activated diffusion-assisted creep deformation can often be described by the Bird-Mukherjee-Dorn (BMD) equation [5].

$$\dot{\varepsilon} = A\frac{DEb}{kT}\left(\frac{\sigma}{E}\right)^{n}\left(\frac{b}{d}\right)^{p} \qquad (3.1)$$

where $\dot{\varepsilon}$ is the steady state strain rate (or minimum creep rate), σ the applied stress, d the grain diameter, A the material dependent constant depending on the operating mechanism, E the elastic modulus, b the Burgers vector, k the Boltzmann's constant ($1.38x10^{-23}$ J/K) , n is the stress exponent, p is the inverse grain size exponent, and D the diffusivity which is described by the equation:

$$D = D_o exp(-Q/RT) \qquad (3.2)$$

where D_o is the pre-exponential constant also known as the frequency factor, Q the appropriate activation energy, R the universal gas constant (8.31 J/K*mol), and T the temperature in kelvin [8]. The BMD equation is a more complex form of the Norton equation used previously for Alloy 709 at 700 °C in chapter 2. The activation energy and diffusivity were not found in this study so values were taken from literature to find the exponents. The creep parameters p, n, and Q are often used to determine the creep mechanism of the material.

$$\frac{\dot{\varepsilon}_m kT}{DEb} = A\left(\frac{\sigma}{E}\right)^n \left(\frac{b}{d}\right)^p \tag{3.3}$$

Comparison of various austenitic stainless steels and Alloy 709 in the framework of such normalization by plotting normalized minimum creep rate against the normalized applied stress. Some studies [3, 9] found stress exponents from the Norton's plots that are higher than the allowable range (5~7) to explain the dislocation climb mainly due to precipitation strengthening or load change creep tests. The larger stress exponents were rationalized by introducing a threshold stress concept due to the added stress introduced by precipitates under creep conditions. Since the data obtained from the monotonic creep tests on Alloy 709 did not result in stress exponents much out of the 5 ~ 7 range the threshold stress approach was determined to not be necessary. It is well known that a stress exponent from 4 to 7 indicates the rate-controlling creep mechanism as dislocation climb. The stress exponents found in this study of Alloy 709 are shown in Figure 3.8. In this study also, we performed a stress change test on Alloy 709 at 600 °C starting at 140 MPa then changing to 125 MPa, back to 140 MPa, then up to 165 MPa. Monotonic creep tests were completed at 600 °C at 140 MPa, 165 MPa and 198 MPa. The minimum creep rate found in the stress change test resulted in faster creep rates at both 140 and 165 MPa. This in turn resulted in a stress exponent of 10.2 which is similar to the apparent stress exponent (10.3) recorded by Alomari et al. [3]. It appears that the stress change experiments have a tendency to increase the stress exponent value; however the reason for such behavior is not known at this point. The conjecture is that the creep specimen during the stress change test conducted by Alomari et al. [3] on Alloy 709 could have experienced additional microstructural evolution under such conditions [3]. On the other hand, the monotonic creep test data in the present study were obtained from the initial period of creep tests where microstructural evolution may not have fully started.

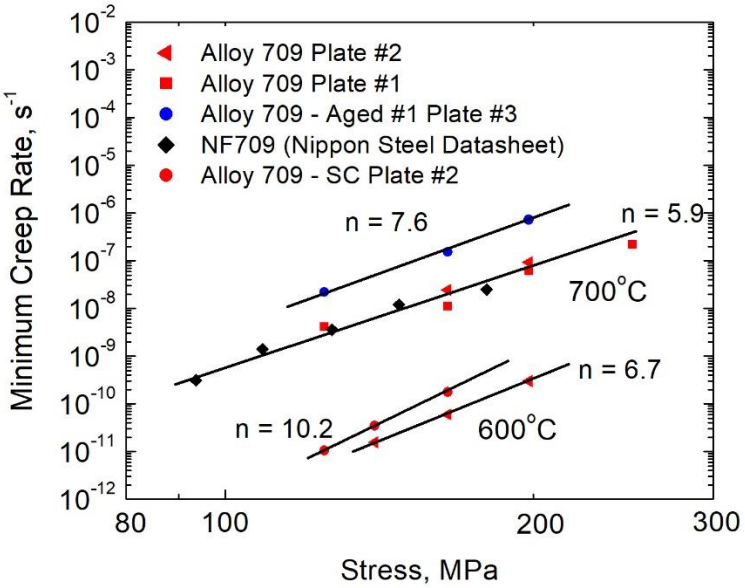

Figure 3.8. Minimum creep rate with the applied stress showing the stress exponents for the various conditions.

Table 3.2. Parametric dependence of various diffusion-controlled deformation mechanisms [10].

Creep Type	***n***	***p***	***Q***
Nabarro-Herring	1	2	Q_L
Coble	1	3	Q_{GB}
Harper-Dorn	1	0	Q_L
Grain Boundary Sliding	2	2	Q_{GB}
Solute Drag Dislocation Creep	3	0	Q_S
Dislocation Climb Creep	4-7	0	Q_L
Low Temperature Climb Creep	7	0	Q_C

where Q_L is lattice diffusion, Q_{GB} is grain boundary diffusion, Q_C is dislocation core diffusion, and Q_S is solute diffusion.

Since only two temperatures were studied in this investigation, there is not enough data to determine the activation energy of Alloy 709. There is however significant data found in literature that allows a good approximation of the activation energy of Alloy 709. Diffusion in FCC alloys is well documented by Abe et al. [11] giving an activation energy of 284 kJ/mol and a D_o of 1.7×10^{-4} m^2/s for Fe diffusing in Fe-20Cr-25Ni/Nb [11]. A value of the Burgers

vector is taken to be 2.5×10^{-10} m. The moduli of elasticity at 600 and 700 °C were found in Nippon Steel's NF709 datasheet to be 1.56×10^{11} Pa and 1.49×10^{11} Pa, respectively [12]. These values were used in this study to assist in finding the mechanism of creep in Alloy 709.

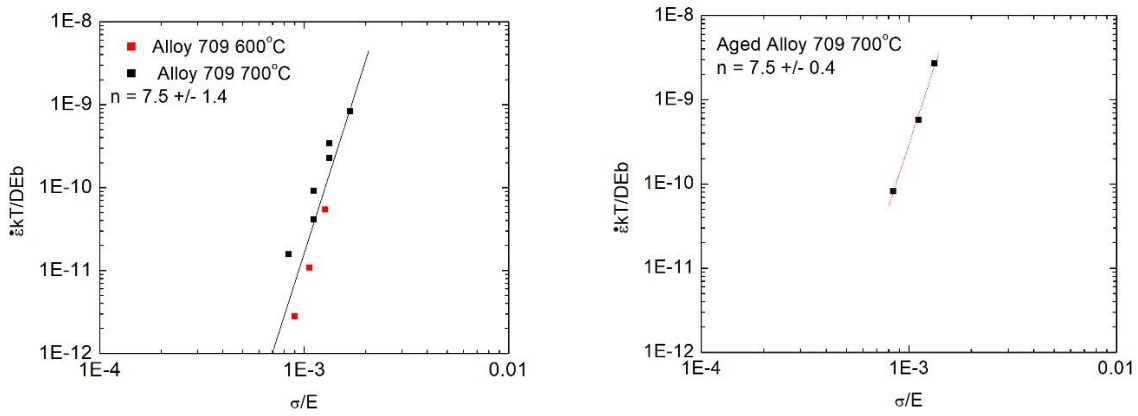

Figure 3.9. BMD plots of the normalized steady state creep rate with the effective stress (a) as-received Alloy 709 crept at 600°C and 700°C and, (b) aged Alloy 709 crept at 700°C.

The BMD normalization of both the aged and as-received Alloy 709 showed a stress exponent of around 7.5. However, the aged Alloy 709 lost creep strength. This suggests that despite aging, the mechanism of creep for Alloy 709 remained in the dislocation climb region of 5 to 7. TEM and optical microscopy are being completed to determine what precipitates or microstructural changes occurred during the aging process. The BMD relation for Alloy 709 is compared with data from variations of 316 SS. For the calculations a D_o of $1.2\text{x}10^{-6}$ m^2/s was used along with an activation energy of 229 kJ/mol [11]. The Burger's vector calculated for Alloy 709 was also used for the 316 SS calculations, the elastic modulus for 316 at 700 °C is not well documented so the one of Alloy 709 at 700 °C was used (1.49×10^{11} Pa). Little variation is observed between Alloy 709 and 316 SS or 316H with this method however Alloy 709 at 600 °C and 700 °C in this study showed slightly better creep strength then the others. The aged Alloy 709 showed worse creep resistance then the 316 counterparts. The stress change test completed by Alomari et al. on Alloy 709 could be experiencing additional precipitation strengthening with the use of stress change tests [3].

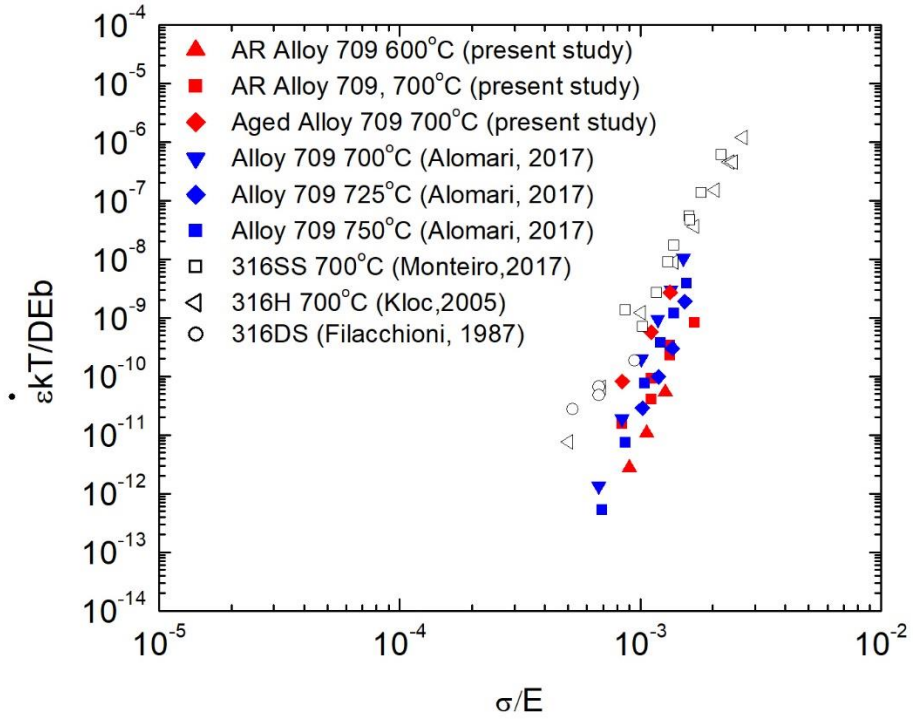

Figure 3.10. Comparison of normalized minimum creep rate with the normalized stress data for different austenitic stainless steels and Alloy 709 [3], [13], [14].

The current results found in this study and the results found by Alomari et al. [3] suggest the creep mechanism of Alloy 709 can be largely described as dislocation climb creep. Thus, the constitutive equation for the as-received Alloy 709 becomes Eqn. 3.4.

$$\frac{\dot{\varepsilon}_{ss}kT}{DEb} = 8.3x10^{11}\left(\frac{\sigma}{E}\right)^{7.5\pm1.4} \quad (3.3)$$

3.5 Conclusion and future work

This study was performed on Alloy 709 to aid in characterizing a potential material for Sodium-cooled Fast Reactors (SFR). Creep tests were performed at 600 °C and 700 °C on as-received Alloy 709. Additional creep tests were completed on aged Alloy 709 at 700 °C. The BMD relation was used to fit the creep tests and resulted in a stress exponent of 7.5 ± 1.4. This alludes to Alloy 709 having a creep mechanism of dislocation climb creep at these temperatures and stresses. This agrees with other studies on Alloy 709 despite not taking the threshold stress approach. Large and fine MX precipitates were observed along $M_{23}C_6$ plates after thermal aging at 700 °C temperatures.

A second batch of aged Alloy 709 (650 °C for 6 months) is to be studied. Potential stress change tests could be studied to determine how a stress change test affects the creep mechanism and life of the material. Additional microstructural analysis is necessary to understand the microstructural effect on the creep properties.

3.6. References

[1] S. Sham, "Advanced Reactor Concepts Program ARC Materials Development - Accomplishments and Plans," 2013.

[2] Z. Kuboň, Š. Stejskalová, and L. Kander, "Effect of Sigma Phase on Fracture Behavior of Steels and Weld Joints of Components in Power Industry Working at Supercritical Conditions," Austenitic Stainl. Steels - New Asp., 2017.

[3] A. S. Alomari, N. Kumar, and K. L. Murty, "Investigation on Creep Mechanisms of Alloy 709," ASME 2017 Nucl. Forum, p. V009T02A003, 2017.

[4] Y. Zhao, J. Zhao, and X. Li, "Microstructural evolution and change in hardness during creep of NF709 austenitic stainless steel," Acta Metall. Sin. (English Lett., vol. 24, no. 3, pp. 220–224, 2011.

[5] T. Shrestha, M. Basirat, I. Charit, G. P. Potirniche, and K. K. Rink, "Creep rupture behavior of Grade 91 steel," Mater. Sci. Eng. A, vol. 565, pp. 382–391, 2013.

[6] T. Sourmail and H. K. D. H. Bhadeshia, "Microstructural evolution in two variants of NF709 at 1023 and 1073 K," Metall. Mater. Trans. A, vol. 36, no. 1, pp. 23–34, 2005.

[7] A. F. Padilha and P. R. Rios, "Decomposition of austenite in austenitic stainless steels," ISIJ Int., vol. 42, no. 4, pp. 325–327, 2002.

[8] S. McCormick, "Effect of heat treatment and creep deformation on the microstructural characteristics of ATI 20-25+Nb austenitic stainless steel," University of Idaho, 2015.

[9] T. Shrestha, M. Basirat, I. Charit, G. P. Potirniche, K. K. Rink, and U. Sahaym, "Creep deformation mechanisms in modified 9Cr-1Mo steel," J. Nucl. Mater., vol. 423, no. 1–3, pp. 110–119, 2012.

[10] I. Charit and K. L. Murty, "Creep behavior of niobium-modified zirconium alloys," J. Nucl. Mater., vol. 374, no. 3, pp. 354–363, 2008.

[11] F. Abe, T.-U. Kern, and R. Viswanathan, Creep-resistant steels, 1st ed. The Institute of Materials, Minerals, and Mining, 2008.

[12] “Nippon steel material data sheet NF709,” Nippon STEEL SUMITOMO Met. Corp., pp. 10–12, 2013.

[13] L. Kloc and J. Fiala, “Viscous creep in metals at intermediate temperatures,” Kov. Mater, vol. 43, no. 2, pp. 105 – 112, 2005.

[14] S. Monteiro Neves, F. Santos, W. Anacleto, and L. Paulo, “Creep Parameters and Dislocation Substructure in AISI 316 Austenitic Stainless Steel From 600oC to 800oC,” Mater. Res., no. 1, pp. 1–5, 2017.

Chapter 4. Microstructural Studies of Crack Profiles of Alloy 709 after Fatigue and Creep-Fatigue Crack Growth Testing at 700°C

Martin Taylor, Nick Shaber, Harry Pugesek, Jose Ramirez, Robert Stephens, Gabriel Potirniche and Indrajit Charit

Abstract

Understanding the creep-fatigue crack growth behavior is essential for long term structural applications in nuclear reactors. Extending the reactor service life beyond sixty years will increase the likelihood of creep-fatigue failures of structural components. The large majority of service conditions in advanced nuclear reactors are likely to involve a combination of creep and fatigue loading. Understanding how the microstructure behaves under these conditions can help in predicting the service life of the material. In this study, an Alloy 709 was used as the experimental material. Fatigue crack growth or FCG (15 Hz at stress ratio, *R* of 0.1) and creep-fatigue (60 s holds at *R* of 0.1) crack growth or CFCG tests of the as-received Alloy 709 specimens were conducted on compact tension (CT) specimens at 700 °C. Transgranular crack growth was dominate for both the FCG and CFCG tests. Comparison of the FCG and CFCG was completed using optical microscopy, EBSD misorientation maps and grain boundary angle maps. The da/dN with ΔK plot revealed that the inclusion of creep hold time between fatigue cycles did not shorten the overall life of Alloy 709 compared to pure fatigue under these conditions. However, the microstructure of the crack profile showed more damage on the CFCG specimen by means of secondary cracks forming and additional subgrain boundaries forming at the edge of the cracks.

4.1. Introduction

Many power plants are required to operate under a wide variety of mechanical and thermal loading conditions. Therefore, the life of the material in-service often experiences cyclic loading at high temperatures. The cyclic loading leads to an interactive creep-fatigue failure mechanism that is often known to accelerate the failure of the component compared to the component under static creep [1]. In order to incorporate a higher degree of reliability, it is crucial for power plants to have a good understanding of how a material will behave under such conditions.

Extending the nuclear reactor service life to 60+ years will increase the likelihood of creep-fatigue failures of structural components [2]. Testing components in the laboratory is critical in

understanding the mechanics of creep-fatigue damage. Considerable work in the area of creep-fatigue characterization has taken place on various stainless steel power plant materials [1, 3], [4]. A recently developed austenitic stainless steel Alloy 709 based on a base composition of Fe-20Cr-25Ni (wt%) that is being considered in various high temperature reactor applications. However, creep-fatigue crack growth behavior is not understood well. The aim of this study is to understand the microstructure around the cracks for both fatigue and creep-fatigue crack growth specimens (FCG and CFCG) of Alloy 709 at 700 °C.

4.2. Material and procedures

An Alloy 709 plate with dimensions of 101.6 mm × 228.6 mm × 20.3 mm was received from the Oak Ridge National Laboratory (ORNL). The prior history of the as-received plate included hot-processing (forged and rolled) and annealing at 1100°C, followed by water-quenching. The chemical composition of the Alloy 709 plate is given in Table 4.1.

Table 4.1. Chemical composition (in wt%) of Alloy 709

C	Mn	Si	P	S	Cr	Ni	Mo	N	Ti	Nb	B	Fe
0.067	0.90	0.40	<0.005	<0.001	19.80	25.09	1.50	0.15	<0.01	0.26	0.0043	Bal.

The specimen geometry chosen was the standard compact tension specimen (CT specimen), with a width, W = 50 mm, thickness, B = 12.5 mm, and an initial notch, a_o = 16 mm, Figure 4.1. The dimensions chosen are in accordance with ASTM Standard 2760, Creep-Fatigue Crack Growth Testing. The CFCG and FCG tests were conducted using a servo-hydraulic MTS test machine shown in Figure 4.2. The CT specimens were side-grooved 4% on each side with 60degree V-notch to prevent crack front tunneling at elevated temperature. The CT specimens were then pre-cracked at room temperature from an initial notch length of approximately 16 mm to a crack length which ranged between 20-22 mm (a/W = 0.40-0.42) from one specimen to another. Direct current potential drop (DCPD) and compliance methods were used to monitor crack length during testing. Compliance was measured using high temperature extensometers with 150 mm long ceramic arms that were attached to the notched region of the CT specimen. Both tests were carried out at 700 °C at a load ratio, R = 0.1. The starting ΔK levels were around ΔK = 19-22 MPa√m and the tests were terminated at a ΔK of approximately 45 MPa√m. The FCG test was run at a frequency of 15 Hz, and the CFCG had a 60 s hold time. After the tests

were stopped, the specimen was cooled to room temperature and subsequently cyclically loaded to break the specimen. This procedure allowed the initial crack length and final crack length to be measured accurately and correlated to the measured PD voltage.

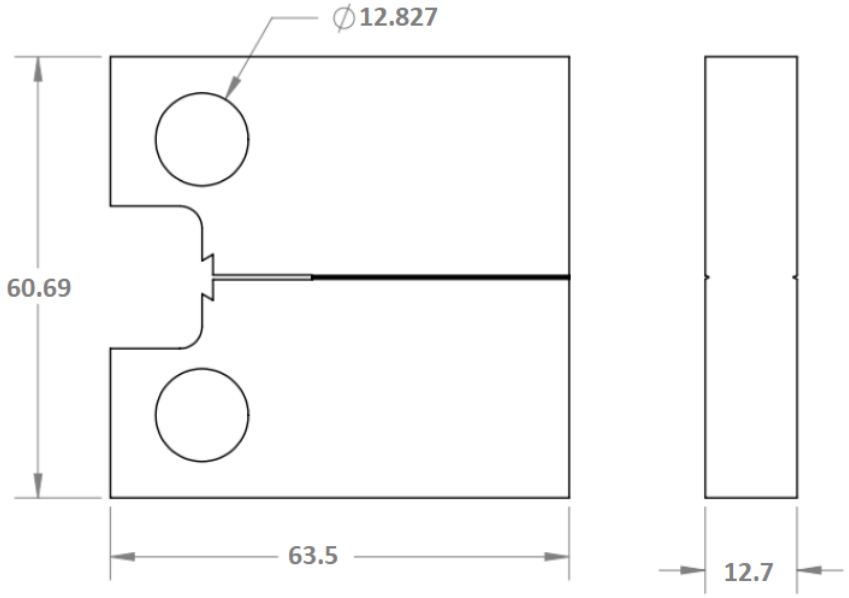

Figure 4.1. CT specimen geometry (all dimensions are in mm).

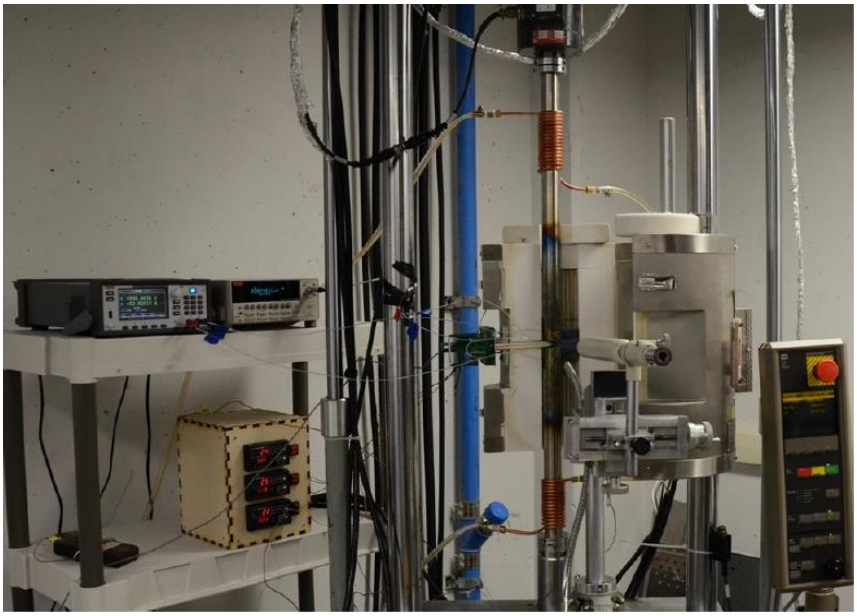

Figure 4.2. The servo-hydraulic MTS test frame used for FCG and CFCG tests.

Sections from the Alloy 709 plate were cut and mounted in acrylic for microstructural characterization of the as-received Alloy 709. One half of the post-test CT specimens were

taken and 5 cuts were made with a diamond wafering blade using a Buehler IsoMet® 1000 saw for metallographic preparation.

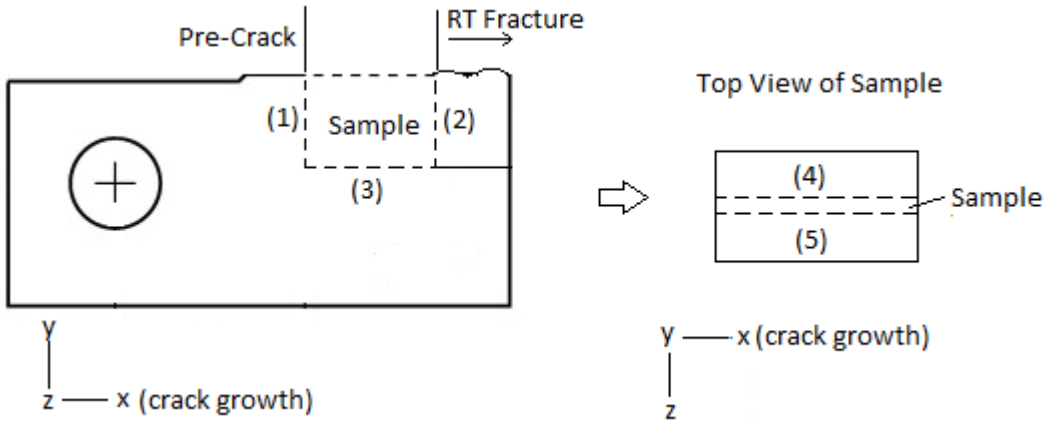

Figure 4.3. Cuts made for FCG and CFCG profile micrographs

Standard metallographic procedures involving sequential grinding and polishing were carried out. The samples were first hot mounted and were then polished to a 0.3 µm surface finish using alumina paste. Optical micrographs were taken of the crack profile pre-etching and after they were electrolytically etched with 10% (by mass) oxalic acid in deionized (DI) water at 6 V for 6-10 s, depending on the surface area of the specimen of interest [5]. Optical microscopy was conducted using an Olympus PMG-3 light microscope. The average grain size was determined from the obtained metallographic images using the mean linear intercept technique.

Electron backscatter diffraction (EBSD) was obtained by grinding the back side of the crack face until the sample was under 200 µm thick. A Gatan disk punch was used to create 3 mm diameter semi-circles that were then ion-milled with argon ions using a PIPS II model 695 machine held at an energy of 4 keV for 5 min, 2 keV for 5 min, and 0.5 keV for 8 min. The surface-prepared disks were placed in the Zeiss Supra 35 FEG-SEM fitted with the QUASOR^{TM} EBSD system. The sample stage was set at an angle of 70° with a working distance of about 16.5 mm. The SEM was operated at an accelerating voltage of 20 kV and put on high current mode. A binning of 4 pixel × 4 pixel was used in this study to obtain high enough resolution.

4.4 Results and discussion

4.4.1 As-received microstructure of Alloy 709

The microstructure of the as-received Alloy 709 consists of near equiaxed grains accompanied by a relatively high density of annealing twins. Grain sizes measured in all three orthogonal planes did not exhibit any significant difference and the mean grain size is estimated to be 38 ± 3 μm. Figure 4.4 shows the as-received microstructure along with an EBSD map of the as-received microstructure. The as-received EBSD map shows randomly oriented equiaxed grains with the presence of twins.

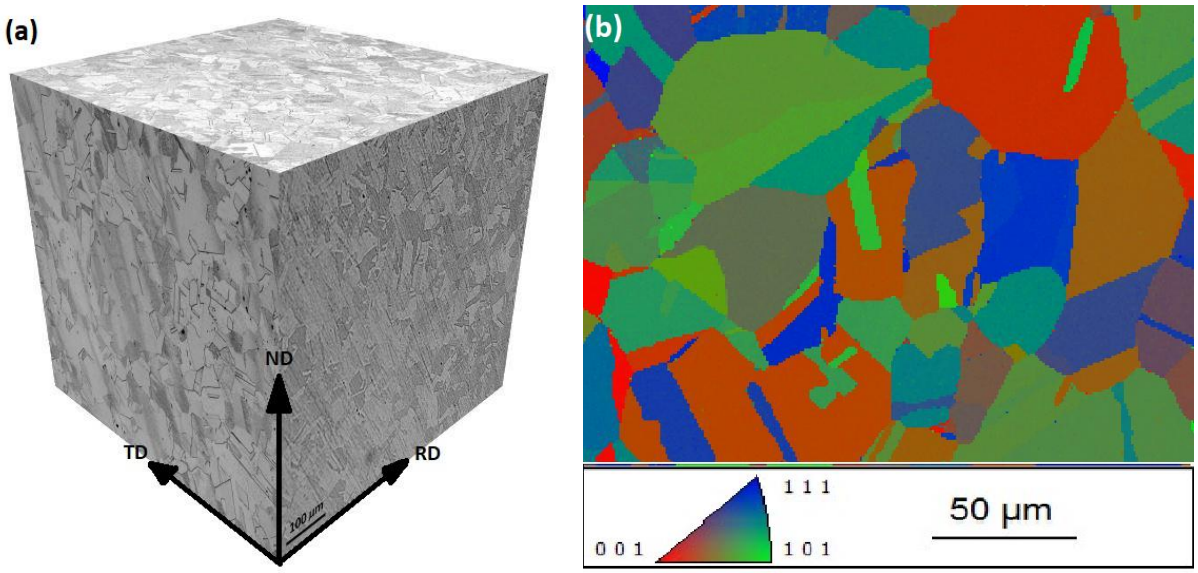

Figure 4.4. (a) As-received microstructure with 38 ± 4 μm grains, (b) as-received EBSD misorientation map.

4.4.2. FCG and CFCG at 700 °C

Figure 4.5 shows the crack growth rate (da/dN) as a function of the stress intensity factor term (ΔK) for one FCG and one CFCG tests conducted at 700 ºC. It appears that the addition of creep hold time had only little impact on the crack growth rate of the material. As seen in Figure 4.7, at lower ΔK the creep-fatigue crack grows slightly faster than the fatigue crack grows. However, at higher ΔK regime, the creep-fatigue crack grows at a slower rate. For theses specimens, it appears the effect of creep on Alloy 709 potentially blunts the crack tip slowing the crack growth at the higher ΔK regime. The current metallographic study was carried out on specimens after they have been ruptured so crack blunting could not be seen; however, the CFCG specimen crack profile has a significant increase in secondary cracks especially at higher ΔK's.

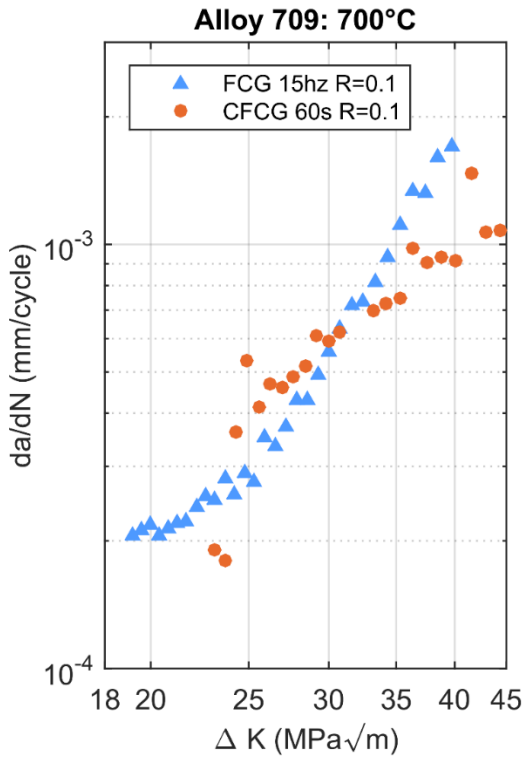

Figure 4.5. Crack growth rate d*a*/d*N* plotted with Δ*K*.

These secondary cracks may decrease the stresses at the crack tip assisting in slowing the crack growth [6]. At lower Δ*K*'s, there are fewer secondary cracks for both the FCG and CFCG samples; so the decrease in the driving force is not as influential on the crack growth. However, at higher Δ*K*'s the secondary cracks in the CFCG sample deceases the driving force of the crack growth more than the increase in crack growth due to creep. This ultimately slows the crack growth in the CFCG at higher Δ*K*'s more than the pure FCG specimen. The optical micrographs show more decorated grains likely due to the time the material was at 700°C allowing precipitate nucleation and growth. Figures 4.6 (a) shows the full crack profile of the FCG and (b) the CFCG tested CT specimens. Enhanced topography or jaggedness for the CFCG profile can be noted compared to the relatively flat profile of the FCG specimen. Crack blunting can be observed in the secondary cracks at higher Δ*K*'s for the CFCG specimen. It is difficult to determine the extent of crack blunting for the primary crack using this method. However the secondary cracks can aid in understanding the nature of the primary crack.

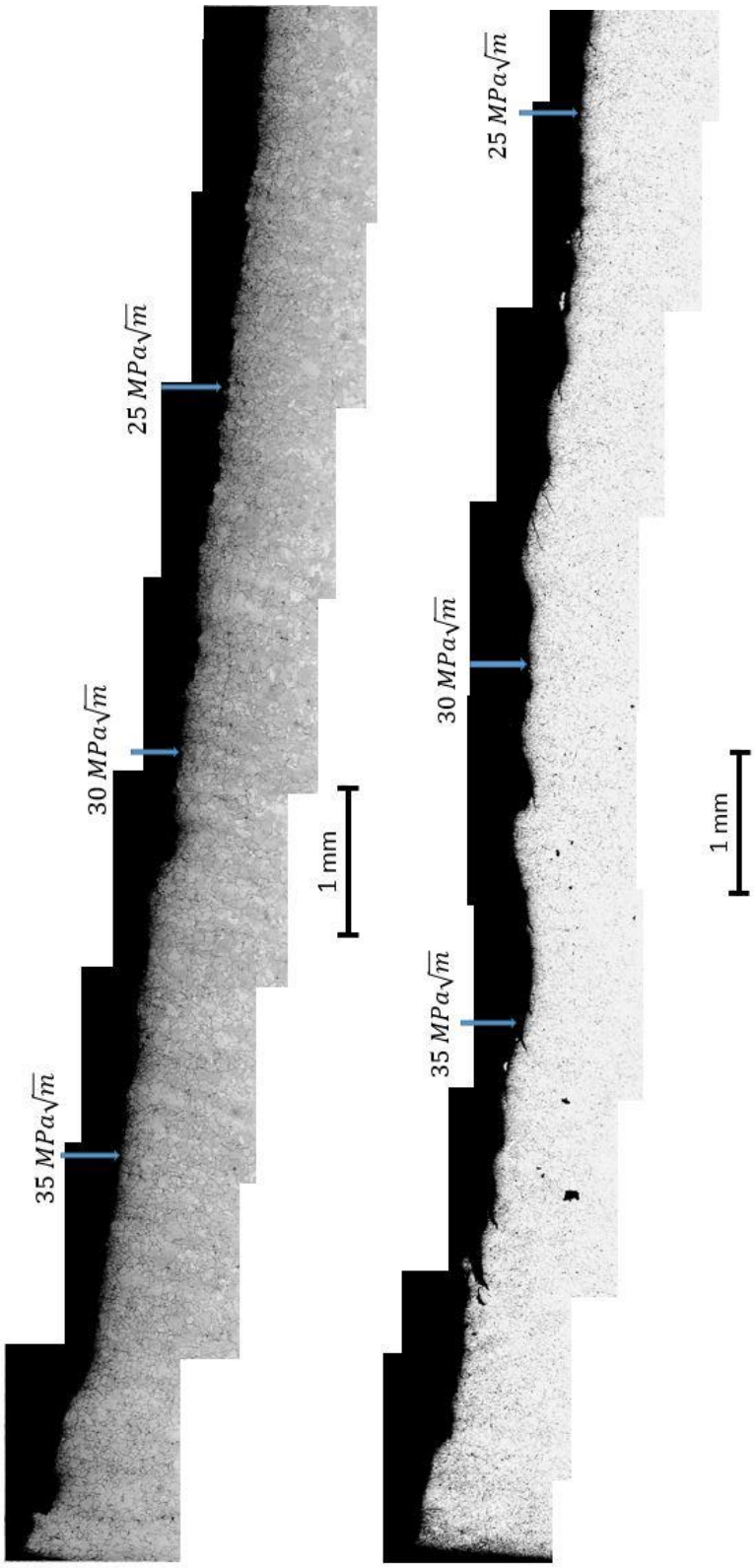

Figure 4.6. (a) Full FCG profile of Alloy 709 at 700 °C at 15 Hz, R = 0.1, (b) full CFCG profile of Alloy 709 at 700 °C at 60 s, R = 0.1.

Closer views of the FCG and CFCG specimens at the location of ΔK = 25 MPa$\sqrt{m}$ are shown in the optical micrographs of Figure 4.7 (a) and (b) respectively, confirming the presence of additional secondary cracks in the CFCG specimen. Note that the crack growth rate of the CFCG specimen was measured to be higher than the FCG specimen in this regime (see Figure 4.5). Figure 4.8 shows the EBSD inverse pole figure maps from the same regions of the specimens albeit at higher magnification. Figure 4.9 (a) and (b) show the grain boundary misorientation maps of the FCG and CFCG specimens. In these figures, the red lines show low angle boundaries (<15^o) and the black lines show the high angle grain boundaries (15^o and above). It can be noted that the formation of new low angle boundaries is noticeably greater and largely concentrated around the CFCG propagated cracks (both the main crack and secondary cracks). These low angle boundaries are subgrain and cell boundaries, which were developed primarily at a ΔK of 25 MPa$\sqrt{m}$ due to the creep hold time [7]. Another important observation from the EBSD maps (both in Figure 4.9 and 4.10) is that the cracks are found to be primarily transgranular in nature with propagated cracks fully within the grains for both the FCG and CFCG samples and not through the grain boundaries.

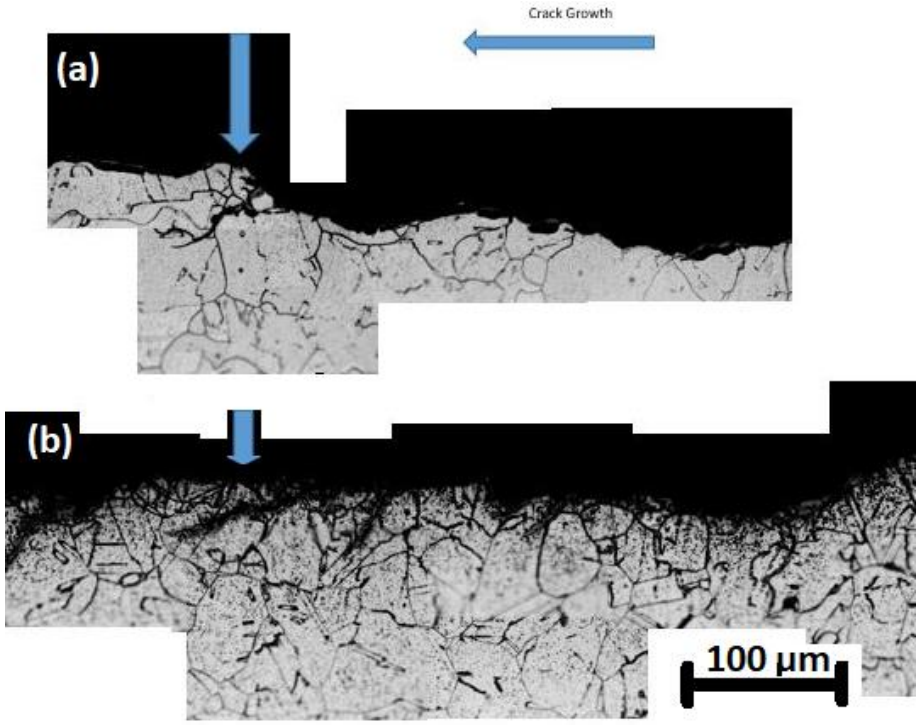

Figure 4.7. (a) FCG of Alloy 709 at ΔK = 25 MPa$\sqrt{m}$ (blue arrow), (b) CFCG of Alloy 709 at ΔK = 25 MPa$\sqrt{m}$.

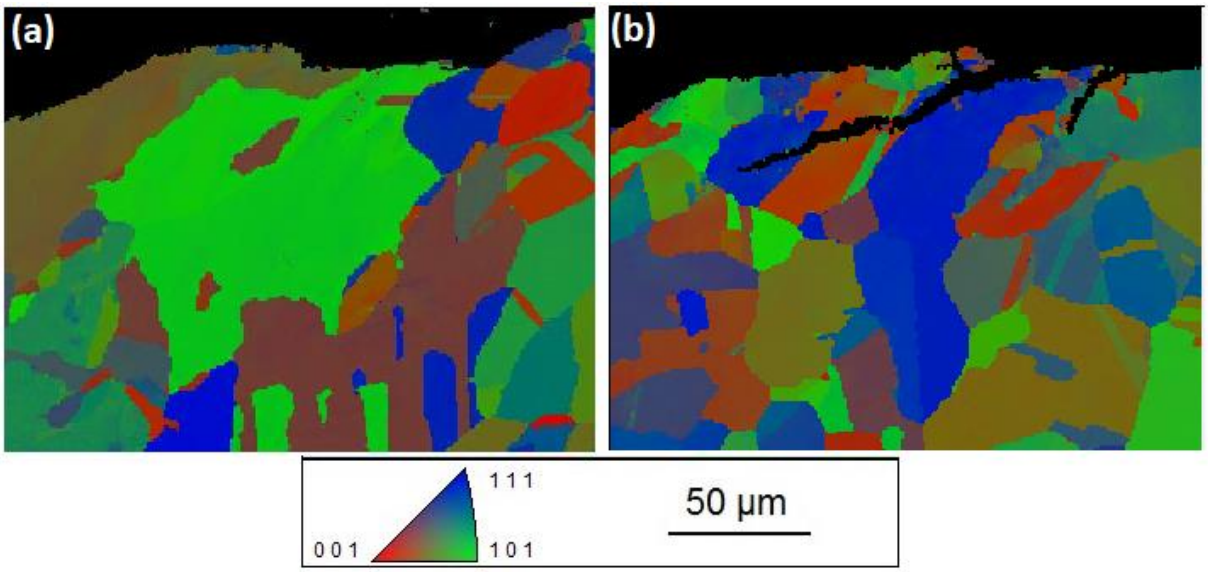

Figure 4.8. EBSD inverse pole figure maps of (a) FCG of Alloy 709 at ΔK = 25 MPa$\sqrt{m}$, (b) CFCG of Alloy 709 at ΔK = 25 MPa$\sqrt{m}$.

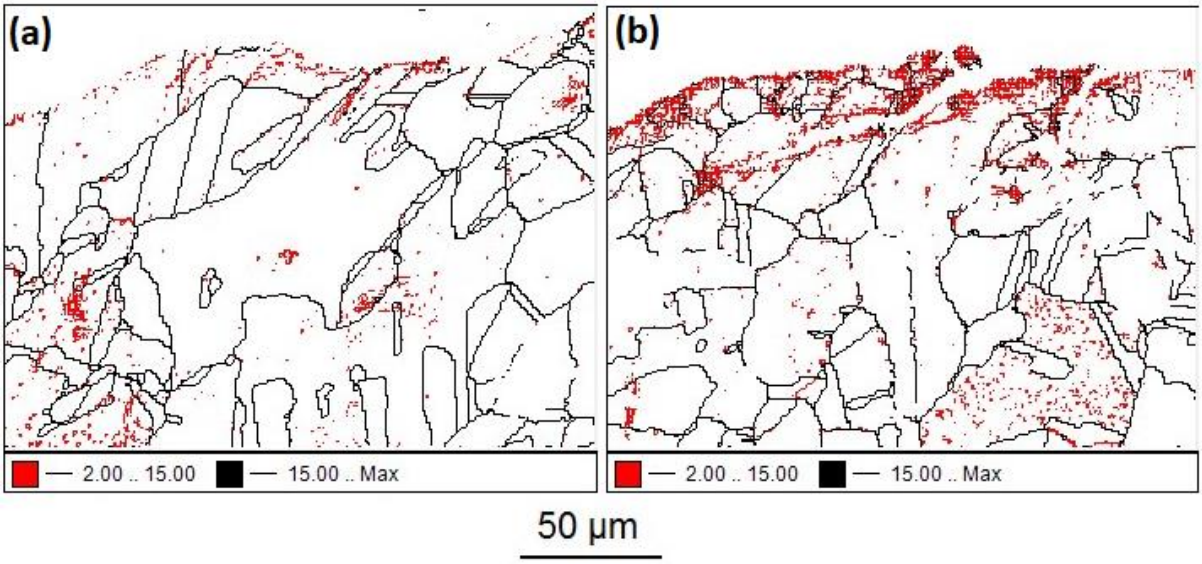

Figure 4.9. EBSD grain boundary misorientation maps: (a) FCG of Alloy 709 at ΔK = 25 MPa$\sqrt{m}$, (b) CFCG of Alloy 709 at ΔK = 25 MPa$\sqrt{m}$.

At a ΔK of 35 MPa$\sqrt{m}$, higher magnification optical images are shown in Figure 4.10 comparing the FCG in (a) with the CFCG in (b). It is important to note that this study compares FCG and CFCG profiles at ΔK's of 25 and 35 MPa$\sqrt{m}$, but the section imaged at a ΔK of 35 MPa$\sqrt{m}$ does not show large secondary cracks but this is not the general trend of the crack at higher ΔK's. It was observed in Figure 4.6 that the frequency and depth of the secondary cracks generally increased with the increase in ΔK. Here also, the inverse pole figures shown in Figure

4.11 exhibits a transgranular fracture mode. Note that a combination of the stage tilt required and low resolution for EBSD mapping resulted inability to resolve the secondary crack on the FCG profile.

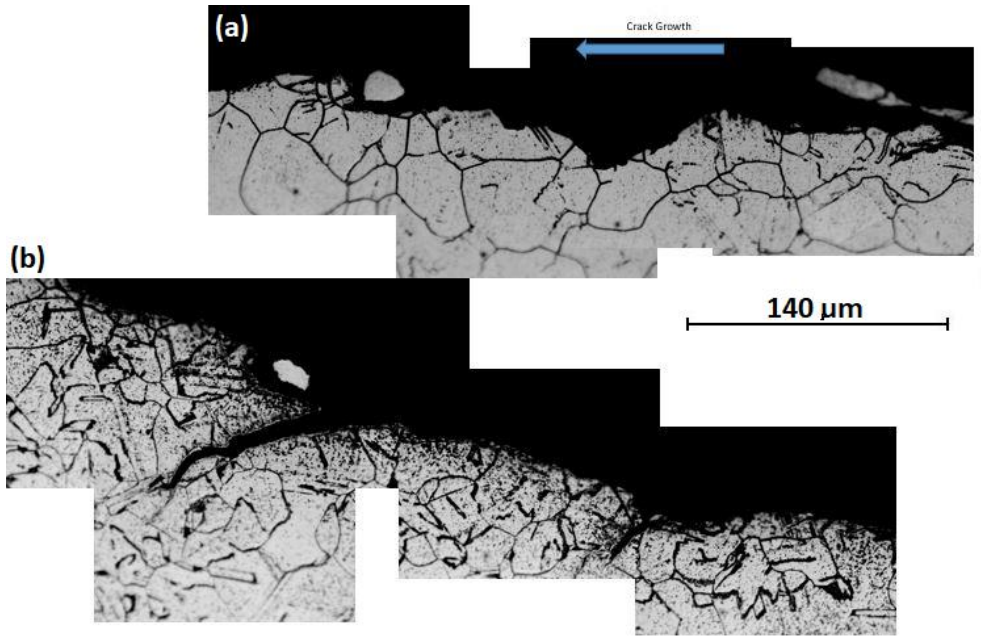

Figure 4.10. (a) Optical microscopy image of cross-section of the FCG of Alloy 709 at ΔK = 35 MPa$\sqrt{m}$ (blue arrow), (b) CFCG of Alloy 709 at ΔK = 35 MPa$\sqrt{m}$.

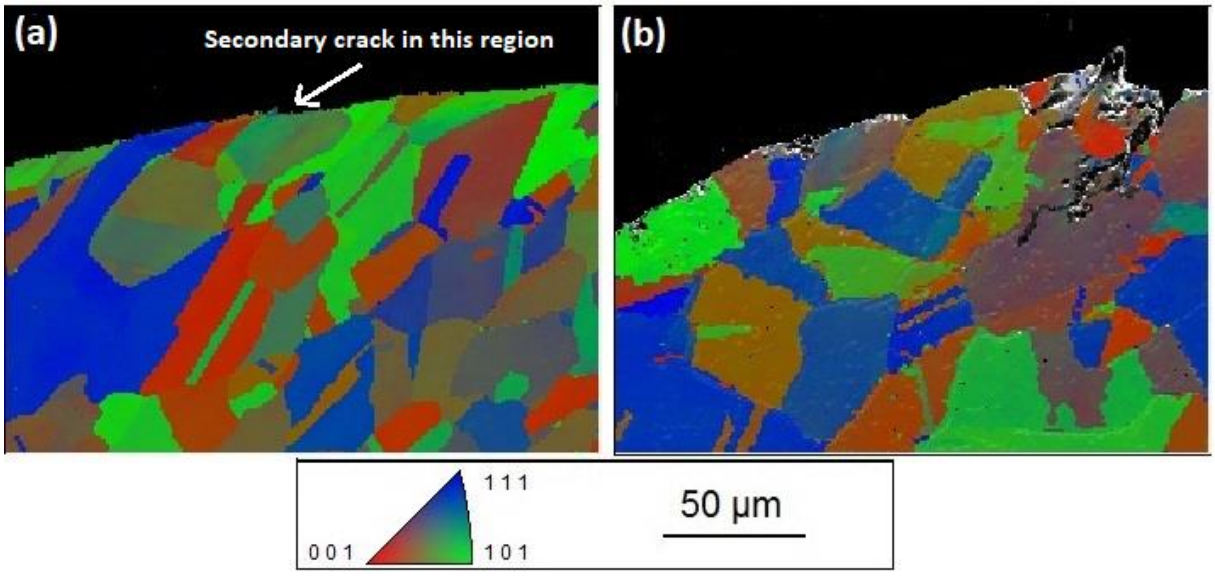

Figure 4.11. EBSD inverse pole figure maps: (a) FCG of Alloy 709 at ΔK = 35 MPa$\sqrt{m}$, (b) CFCG of Alloy 709 at ΔK = 35 MPa$\sqrt{m}$.

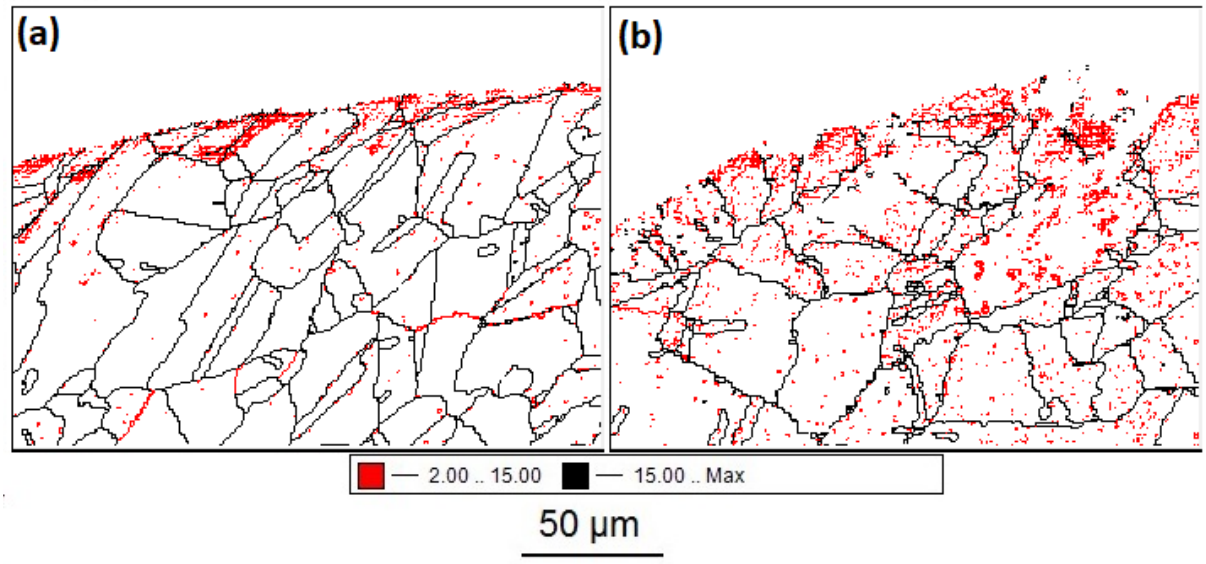

Figure 4.12. EBSD grain boundary misorientation maps: (a) FCG of Alloy 709 at ΔK = 35 MPa$\sqrt{m}$, (b) CFCG of Alloy 709 at ΔK = 35 MPa$\sqrt{m}$.

The grain boundary misorientation maps in Figure 4.12 comparing the FCG in (a) to the CFCG in (b) at a ΔK of 35 MPa$\sqrt{m}$, show an increase in subgrains for both the FCG and CFCG specimens along the crack face. The subgrains at higher ΔK's could be caused by the dislocations piling up at the front of the crack for the FCG specimen [8]. For the CFCG specimen they are likely formed by a combination of the dislocation climb recovery and dislocation pile-up. Further studies need to be done to fully understand why the CFCG of Alloy 709 is slower at higher ΔK's than the FCG. There are studies [7] that suggest subgrains harden the material, which could explain the faster crack growth of the CFCG specimen at lower ΔK's. But at higher ΔK's there appear to be subgrains in both the FCG and CFCG specimens, suggesting the slowing of the crack growth of the CFCG specimen is due to a decrease in the driving force due to a greater extent of secondary cracking and crack tip blunting [7].

4.5 Conclusion

- Alloy 709 exhibits nearly the same crack growth rate when under CFCG for 60 s holds at 700 °C as being under pure FCG at 15 Hz and a R = 0.1 for both.
- Optical microscopy revealed more jagged topography for the CFCG specimen than the FCG test.
- Both FCG and CFCG exhibited transgranular crack growth.

- At ΔK = 25 MPa$\sqrt{m}$, EBSD grain boundary maps show more subgrains forming in the CFCG specimen than the FCG specimen, because of dislocation climb based recovery creep. Further test will be needed to understand these observations.
- The addition of creep slowed the crack growth (da/dN) at ΔK over 30 MPa$\sqrt{m}$.
- At ΔK = 35 MPa$\sqrt{m}$, EBSD grain boundary maps show more subgrains forming in the FCG specimen than what was observed at a ΔK of 25 MPa$\sqrt{m}$.

4.6 References

[1] N. Ab Razak, C. M. Davies, and K. M. Nikbin, "Creep-fatigue crack growth behavior of P91 steels," Procedia Struct. Integr., vol. 2, pp. 855–862, 2016.

[2] T. Allen, J. Busby, M. Meyer, and D. Petti P, "Material challenges for nuclear systems," Materials Today, vol. 13, no. 12. pp. 15–23, 2010.

[3] S. Holdsworth, "Creep-fatigue failure diagnosis," Materials (Basel)., vol. 8, no. 11, pp. 7757–7769, 2015.

[4] R. P. Skelton, "The treatment of very short crack growth in low cycle fatigue and creep fatigue," Mater. High Temp., vol. 32, no. 3, pp. 323–339, 2015.

[5] T. Sourmail and H. K. D. H. Bhadeshia, "Microstructural evolution in two variants of NF709 at 1023 and 1073 K," Metall. Mater. Trans. A, vol. 36, no. 1, pp. 23–34, 2005.

[6] L. Songsong, B. Rui, Z. Ting, and F. Binjun, "Mechanism of crack branching in the fatigue crack growth path of 2324-T39 aluminum alloy," Frat. ed Integrita Strutt., vol. 10, no. 35, pp. 74–81, 2016.

[7] R. Zauter, F. Petry, H.-J. Christ, and H. Mughrabi, "High temperature creep behavior and microstructure development of AISI 304L stainless steel," Mater. Sci. Eng. A, vol. 124, no. 2, pp. 125–132, 1990.

[8] I. Nikulin, T. Sawaguchi, K. Ogawa, and K. Tsuzaki, "Microstructure Evolution Associated with a Superior Low-Cycle Fatigue Resistance of the Fe-30Mn-4Si-2Al Alloy," Metall. Mater. Trans. A Phys. Metall. Mater. Sci., vol. 46, no. 11, pp. 5103–5113, 2015.

Concluding Remarks

The present work reported the results and analyses of a preliminary investigation of the creep behavior, microstructural analysis, and FCG and CFCG crack profile analysis of Alloy 709 that is currently being considered for use as a structural material for the sodium fast reactor. The following observations and conclusions were made:

- At 700°C, Alloy 709 experienced slight dynamic strain aging with a yield strength of around 180 MPa and an ultimate tensile strength of about 450 MPa.
- Accelerated creep tests at 700 °C showed a brief primary, short secondary, and long tertiary zone.
- Norton plots of the creep tests resulted in a stress exponent of ~6, suggesting the most likely rate-controlling creep mechanism to be dislocation climb. However, further creep test data is needed to unambiguously determine the operating micro-mechanism.
- Ductile transgranular fracture surfaces were observed by SEM with dimple-like features from microvoid coalescence. However, the optical microscopy of the longitudinal cross-section did not reveal any cavitation or cracking away from the fracture tip, implying that most of the damage was concentrated in the immediate vicinity of the fracture tip.
- Although optical microscopy did not show subgrain formation, cross sectional results from the EBSD showed low angle grain boundaries (<15°) forming in the gauge section of the 700°C 165 MPa crept specimen. Orientation maps from the EBSD showed significant grain alignment in the gauge section compared to the grip section.
- TEM results confirms subgrain growth and also shows a decrease in precipitates in the gauge section compared to the grip.
- Thermo-Calc was used to find the phases present and will be used for future creep studies on aged Alloy 709.
- Creep tests were performed at 600 °C and 700 °C on as-received Alloy 709.
- Additional creep tests were completed on aged Alloy 709 at 700 °C.
- The BMD relation was used to fit the creep tests and resulted in a stress exponent of 7.5 ± 1.4.

- Alloy 709 has a creep mechanism of dislocation climb creep at these temperatures and stresses.
- This agrees with other studies on Alloy 709 despite not taking the threshold stress approach.
- Large and fine MX precipitates were observed along $M_{23}C_6$ plates after thermal aging at 700 °C temperatures.
- Alloy 709 exhibits nearly the same crack growth rate when under CFCG for 60 s holds at 700 °C as being under pure FCG at 15 Hz and a $R = 0.1$ for both.
- Optical microscopy revealed more jagged topography for the CFCG specimen than the FCG test.
- Both FCG and CFCG exhibited transgranular crack growth.
- At $\Delta K = 25$ MPa$\sqrt{m}$, EBSD grain boundary maps show more subgrains forming in the CFCG specimen than the FCG specimen, because of dislocation climb based recovery creep. Further test will be needed to understand these observations.
- The addition of creep slowed the crack growth (da/dN) at ΔK over 30 MPa$\sqrt{m}$.

Future Work

Further characterization of Alloy 709 will be completed to fully understand the microstructure, creep, FCG, and CFCG. The thermal aging schedule of 3 and 6 months at 650^{o}C was not applied until late in the project due to computational restrictions. The aged material will assist in understanding the microstructure and mechanical properties of Alloy 709 after being exposed to service temperatures for 25 and 50 years.

- Microstructural analysis on aged 3 and 6 months at 650°C, including optical, TEM, SEM, and EBSD.
- Creep tests on third plate Alloy 709 as received, aged #1 and aged #2.
- Further microstructural studies on the crack profiles of FCG and CFCG.

Appendix

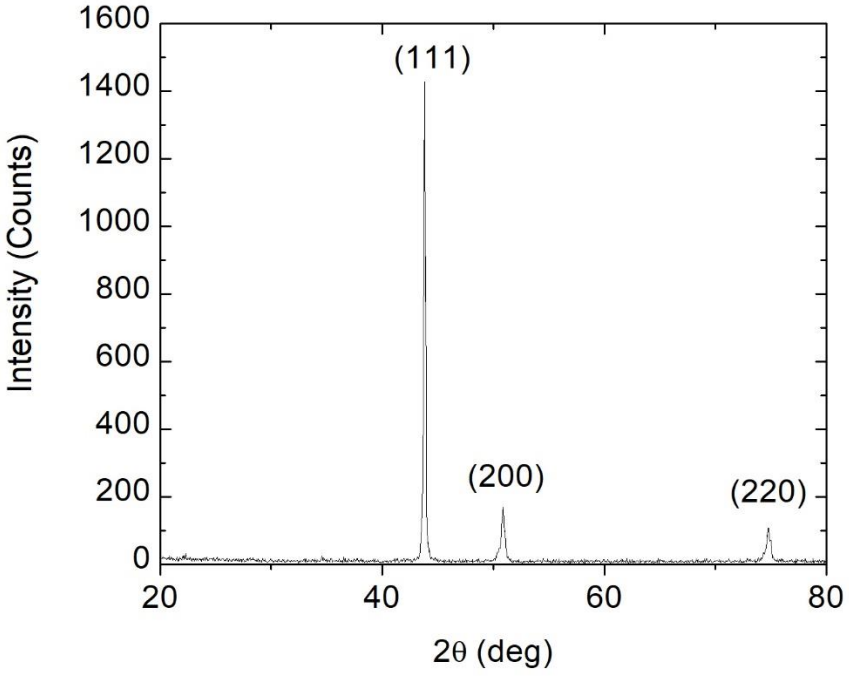

Figure A.1. The XRD pattern of the bulk Alloy 709.

Figure A.1 shows the XRD pattern of the as received Alloy 709. We would like to use Bragg law to calculate the lattice constant of Alloy 709. The Bragg law is given as:

$$\lambda = 2\, d_{hkl}\, sin(\theta) \qquad \text{(A1)}$$

where λ is the wavelength of the X-rays used, d_{hkl} is the interplanar spacing and θ is the Bragg angle. On the other hand, the interplanar spacing the calculation of the lattice parameter (a) by the following relation:

$$d_{hkl} = \frac{a}{\sqrt{h^2+k^2+l^2}} \qquad \text{(A2)}$$

The three major peaks in the diffraction pattern of Figure 22 are created due to the austenitic matrix of Alloy 709 at the following 'θ' angles of 21.9º, 25.45º, and 37.39º, respectively. Using the Eqns. (A1) and (A2), we get the following lattice constants of 0.3577 nm, 0.3585 nm, and 0.3588 nm. Averaging the three calculated three lattice gives a lattice constant of 0.3583 nm. This value was then used to find the Burgers vector magnitude by the relation for FCC:

$$|b| = \frac{a}{2}\langle 110\rangle = \frac{a}{2}\sqrt{1^2 + 1^2 + 0^2} = \frac{a}{\sqrt{2}} \qquad \text{(A3)}$$

Differential Scanning Calorimetry (DSC) was carried out on Alloy 709. DSC measures the heat flow as a function of temperature associated with exothermic and endothermic transitions. A NETZSCH STA 409 PC was used to run a test of 5°C per min up to 1400°C. The energy associated with precipitation is something that can be calculated from DSC results heating rates.

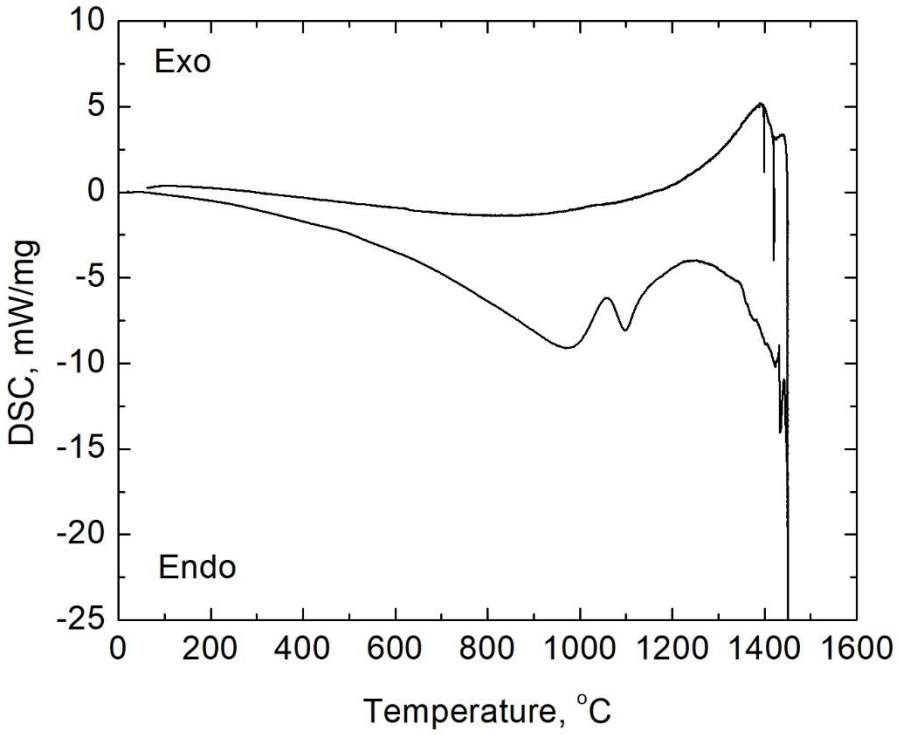

Figure A.2. DSC curve of Alloy 709 showing the endothermic and exothermic peaks.

A summary of the monotonic creep tests completed on the three heats of Alloy 709 are given in Table A.1, showing the temperature, stress, minimum creep rate ($\dot{\varepsilon}_{min}$), time to rupture, and the percent elongation at rupture (ER).

Table A.1. Summary of the creep test completed.

First Plate (Heat 011502-H5)				
Temperature (ºC)	**Stress (MPa)**	$\dot{\varepsilon}_{min}$ **(s^{-1})**	**Time to Rupture (h)**	**ER (%)**
700	125	4.17×10^{-9}	N/A	N/A
700	165	1.1×10^{-8}	1128	78
700	198	6.1×10^{-8}	407	65
700	250	2.2×10^{-7}	99	59
Second Plate (Heat 11594-3)				
Temperature (ºC)	**Stress (MPa)**	$\dot{\varepsilon}_{min}$ **(s^{-1})**	**Time to Rupture (h)**	**ER (%)**
700	165	2.45×10^{-8}	N/A	N/A
700	198	9.17×10^{-8}	337	76
600	140	1.56×10^{-11}	N/A	N/A
600	165	6.00×10^{-11}	N/A	N/A
600	198	3.03×10^{-10}	N/A	N/A
Third Plate (Heat 58776-4, Aged 3 Months at 650ºC)				
Temperature (ºC)	**Stress (MPa)**	$\dot{\varepsilon}_{min}$ **(s^{-1})**	**Time to Rupture (h)**	**ER (%)**
600	198	2.71×10^{-9}	N/A	N/A
700	125	2.19×10^{-8}	N/A	N/A
700	165	1.53×10^{-7}	N/A	N/A
700	198	7.22×10^{-7}	82	69
Third Plate (Heat 58776-4, Aged 6 Months at 650ºC)				
Temperature (ºC)	**Stress (MPa)**	$\dot{\varepsilon}_{min}$ **(s^{-1})**	**Time to Rupture (h)**	**ER (%)**
700	165	3.02×10^{-7}	N/A	N/A
700	198	1.26×10^{-6}	51	58

Tensile tests were performed at a strain rate of 10^{-3} s^{-1} on the as-received and aged (3 and 6 months at 650ºC) Alloy 709 at 600ºC and 700ºC, shown in Figures A.3 and A.4, respectively.

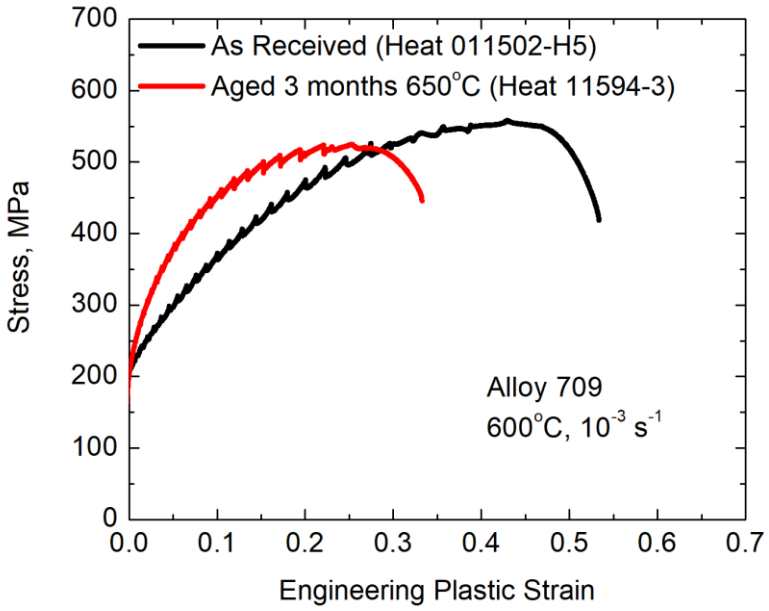

Figure A.3. Engineering stress with the plastic strain at 600°C

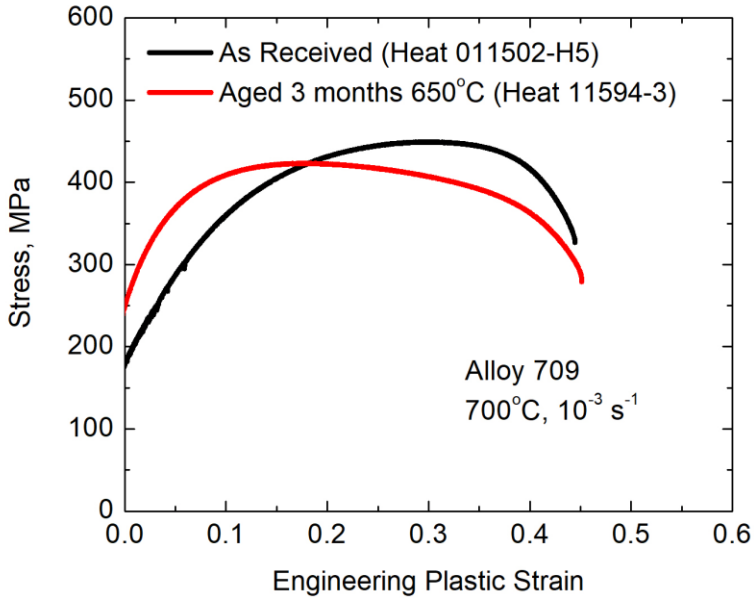

Figure A.4. Engineering stress with the plastic strain at 700°C

Table A.2. Summary of the tensile tests completed.

	600°C As-received	**600°C Aged 3 months at 650°C**	**700°C As-received**	**700°C Aged 3 months at 650°C**
Yield Strength	206 MPa	248 MPa	178 MPa	249 MPa
UTS	558 MPa	525 MPa	449 MPa	423 MPa
Elongation (%)	51%	31%	43%	41%
Reduction in Area (%)	54%	43%	59%	64%
True Stress at Fracture	943 MPa	910 MPa	817 MPa	938 MPa